Disturbance reduction in a moving-magnet linear synchronous motor with a segmented stator

Rovers, J.M.M.

Award date:
2008

TU/e technische universiteit eindhoven

Capaciteitsgroep Elektrische Energietechniek
Electromechanics & Power Electronics

Master of Science Thesis

Disturbance Reduction in a Moving-Magnet Linear Synchronous Motor with a Segmented Stator

J.M.M. Rovers
EPE.2008.A.03

Coaches:

dr.ir. J.W. Jansen, TU/e
dr. E. Lomonova, TU/e
ir. W. Dirkx, Bosch Rexroth Electric Drives and Controls

May 5, 2008

/ faculteit elektrotechniek

Disturbance Reduction in a Moving-Magnet Linear Synchronous Motor with a Segmented Stator

J.M.M. Rovers

Supervisors:
Eindhoven University of Technology
Dr. Ir. J.W. Jansen
Dr. E. Lomonova, M.Sc.

Bosch Rexroth Electric Drives and Controls
Ir. W. Dirkx

June 4, 2008

Abstract

This M.Sc. thesis concerns the electromagnetic analysis and reduction of the force ripples in a moving-magnet linear actuator with a segmented stator. Starting from the system as it is currently under development at Bosch-Rexroth, it has been recognized that the system has several problems which are due either to the control structure or the measurement system (Hall-sensors). To eliminate these problems, the control structure has been changed and a linear encoder has been used for position measurement. This way, the focus has been laid on the problems which are due to the physical layout of the system.

The electromagnetic behaviour of the actuator has been analyzed in detail and it has been recognized that the system under study is, as long as the translator is fully overlapping a stator segment, a balanced three-phase system. However, when the translator does not fully overlap a stator segment, it is not. Moreover, when the translator does not fully overlap a stator segment, the cogging force is significantly large and dominated by a component due to the finite translator length.

Using a (traditional) $dq0$-based switching algorithm, the switching between subsequent stators has been investigated. The disturbances acting on the translator during its motion over the track have been identified. The $dq0$-decomposition is not valid for the entire stroke of the machine and this results in force ripples when using a $dq0$-based switching algorithm. It has been shown that, in the case of the $dq0$-based switching algorithm, there exists an optimal distance between subsequent stators which decreases the force ripple. However, this force ripple is still significant.

To compensate these force ripples, the direct force-current decoupling switching algorithm, which calculates the three-phase currents based on the instantaneous values of the EMF per phase, has been implemented. This switching algorithm also minimizes ohmic losses in the system. To verify the performance of the direct force-current decoupling switching algorithm, both the switching algorithms have been simulated and implemented in a track comprising three stator segments and one translator. The direct force-current decoupling switching algorithm performs better, in terms of the postion accuracy and reduction of the force ripple, than the $dq0$-based switching algorithm. Using the new algorithm, the force ripples can (theoretically) be reduced to zero, independent on the distance between the stator segments, and the position error is significantly reduced.

Contents

Chapter 1

Introduction

This research is part of a joint research project between the Eindhoven University of Technology and the Bosch-Rexroth Electric Drives and Controls Company.

1.1 Company Profile

Bosch Rexroth Electric Drives and Controls - previously Nyquist B.V. - develops and sells high-tech motion control systems for manufacturers that develop high-quality and complex machines in the field of semiconductors, inspection and analysis, medical systems, and complex handling and processing. More specifically, the company offers solutions in drive technology, automation systems and control components. Their systems are (mostly) based on the NYCe4000 system, which is a motion controller with integrated power amplifiers.

1.2 Background

The system under study is a long-stroke positioning system based on linear permanent magnet motors. Traditionally, the linear motion is created using rotary machines and mechanical conversion (e.g. conveyor belts) of the rotating motion into translating motion. Linear motion can also be realized using linear motor. Such positioning systems have several advantages over the traditional systems. For example, they have a low inertia, a high force density, compact design, do not have rotating parts and need low maintenance [1, 2].

Bosch-Rexroth creates such long-stroke positioning systems using permanent-magnet linear synchronous motors (PMLSMs). A permanent-magnet linear synchronous motor consists of a plate with permanent magnets (PMs) mounted on it, and an armature with coils. Usually, the moving part (the translator) is the armature, since then the stationary part (the stator) simply consists of permanent magnets. The consequence of such a moving-coil PMLSM is that the moving part needs to be connected to a power supply to power the coils, which introduces a cable slap and limits the length of the stroke. When using such a motor for a transportation system, this is a disadvantage. The structure can be inverted, in which case the magnet plate is the moving part (and hence does not need a power connection) and the armature is the stationary part.

The fact that the translators do not need to be connected by wires to the power supply makes the system suitable for application in areas like:

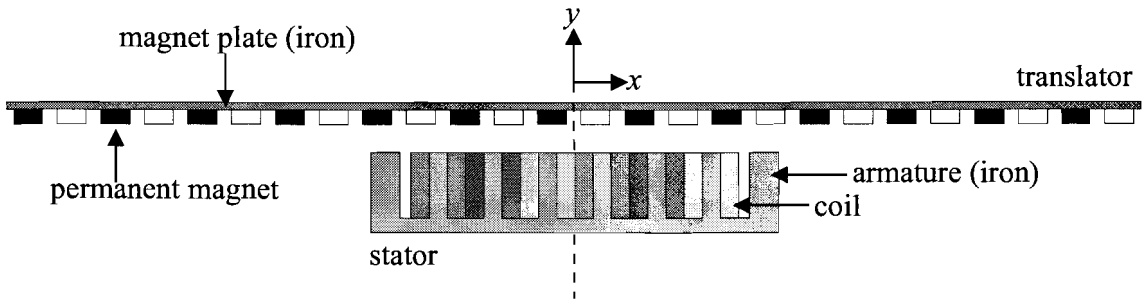

Figure 1.1: Track segment consisting of one translator and one stator.

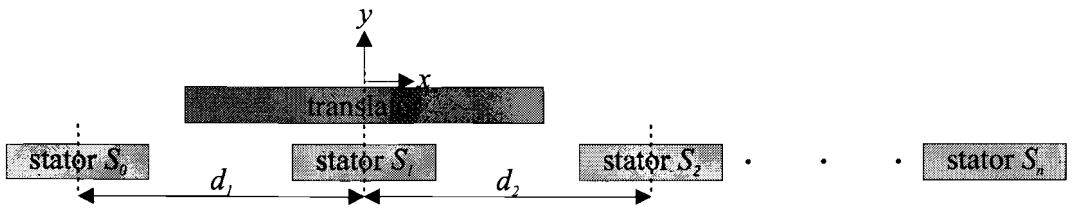

Figure 1.2: Schematic representation of the track, where "stator S_n" a stator segment and d_n the distance between stator segment S_{n-1} and S_n.

- Positioning within a vacuum environment
- Positioning in a dirty environment (i.e. chemicals)
- Positioning in an environment with "high pressure/high temperature" cleaning requirements

The drawback of such a structure is that the track is a continuous array of coils, which significantly increases cost when the stroke length increases. A solution is to use a segmented stator, which means that it comprises several stator segments at a certain distance apart. Figure 1.2 shows a schematic representation of the track, where "stator S_n" is a stator segment and d_n is the distance between stator segment S_{n-1} and S_n. Such a segmented structure allows for multiple translators. Moreover, using a moving-magnet linear synchronous motor with segmented stator allows for complex track layouts, the use of e.g. multiple floors (using elevators) and it is possible to add or remove translators from the track during operation. This makes the moving-magnet linear synchronous motor an interesting alternative for production lines in the high-tech industry.

1.3 Problems

The company is experiencing several problems concerning this system. First, the system which is currently in use is not known in detail. An existing design has been customized and is not being used as was intended. Second, the translator experiences several disturbance forces mainly due to the switching between stator segments. These disturbances result in a (relatively) high position error of the translator. It is unknown whether the causes of these

disturbances are due to a control problem or due to the physical phenomena behind the system.

1.4 Goal

Goal of this project is to analyze the electromagnetic behaviour and improve the performance (in terms of position accuracy and reduction of force ripples) of the system. This M.Sc. thesis starts with a system description in which the system as it is currently under development at Bosch-Rexroth is analyzed and the performance of this system is verified (Chapter 2). Next, an analysis using the finite element method (FEM) of a segment of the structure (comprising one stator and one translator), to investigate the magnetostatic behaviour of the system and to indentify the sources of the force components acting on the translator, is presented (Chapter 3). The control structure is investigated and two commutation algorithm are implemented and compared (Chapter 4) and conclusions and recommendations regarding this system are given (Chapter 5).

Chapter 2

System Description

Bosch-Rexroth currently has long-stroke position systems using PM linear motors under development. They are experiencing several problems concerning the system. To identify these problems, several measurements of the the position error and force acting on the translator are made on the existing system.

2.1 Current situation

The moving-magnet PMLSM under study is constructed of the Tecnotion TL-6N motor as earlier investigated in [3, 4], and is implemented for use as a long-stroke positioning system. A photo of the system as it is currently under development at Bosch-Rexroth is shown in Figure 2.1, where a translator is shown with a magnet plate underneath it and stator segments mounted in the track. The translators are guided using guidance rails and linear roller bearings. The PMLSM has an airgap of 5 mm, instead of the 1 mm airgap it was designed for. A drawing of one segment of the machine is shown in Figure 2.2 and the dimensions of the structure are listed in Table 2.1. Each of the stator segments is equipped with two Hall sensors installed at each end of the block which measure the position of the movers. The magnets are skewed at a 4° angle to decrease cogging.

During the motion of the translator, the stator segments are individually controlled, using the NYCe4000 motion control system, by seperate controllers as illustrated in Figure 2.3. The position of the translator is measured using Hall-sensors. An advantage of such a control structure is that it is easy to add extra stator segments. However, this type of control could

Table 2.1: Specifications of Tecnotion TL-6N PMLSM

	symbol	value
stator length	L_S	118 mm
slot pitch	τ_S	16 mm
pole pitch	τ_P	12 mm
translator length	L_T	320 mm
airgap length	g	5 mm
depth		52 mm
maximum current		6 A

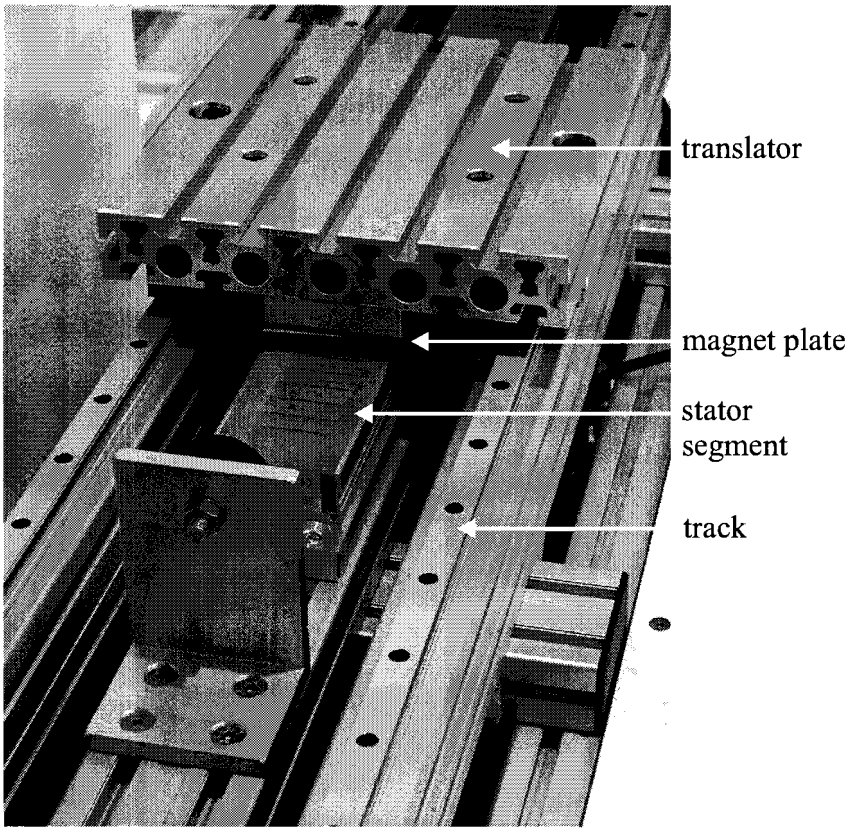

Figure 2.1: Photo of the linear synchronous motor.

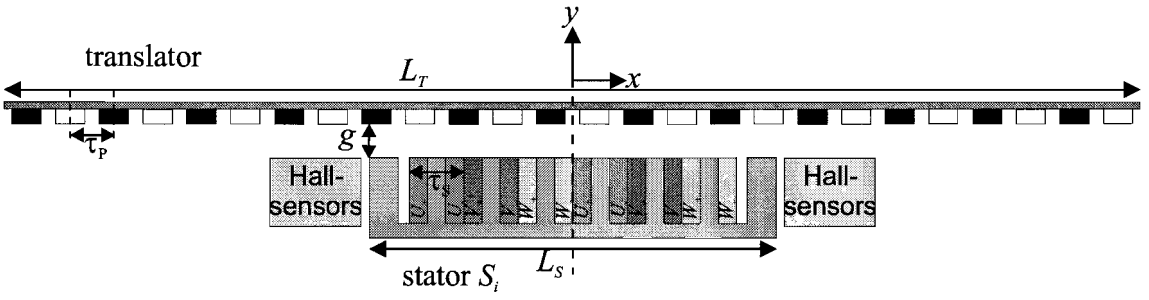

Figure 2.2: Schematic representation of one segment of the PMLSM system.

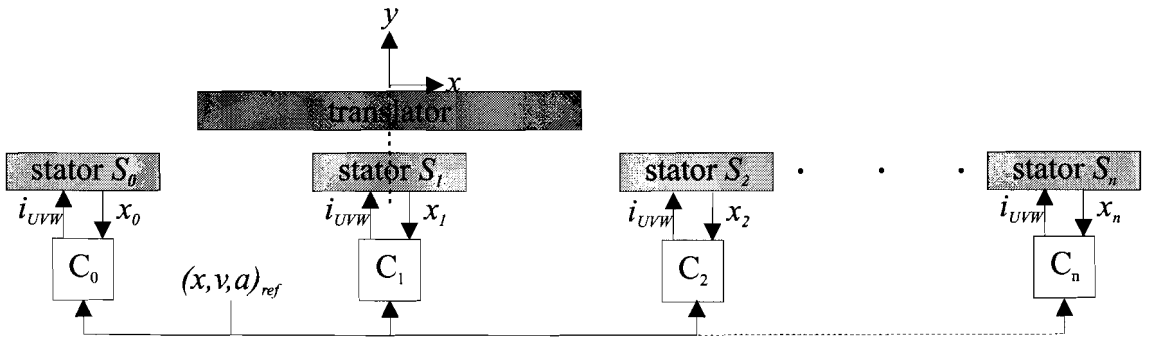

Figure 2.3: Control structure implemented in the Bosch-Rexroth setup.

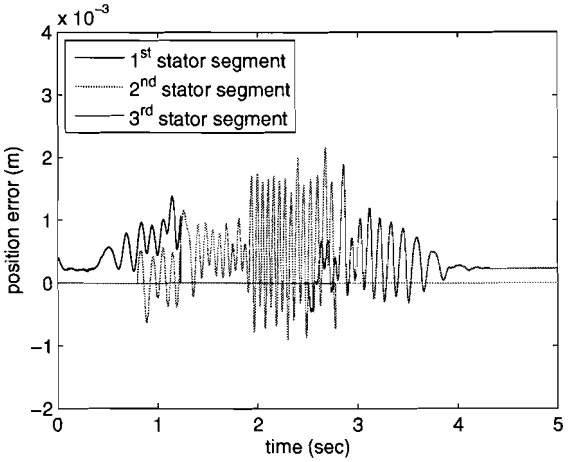

Figure 2.4: Position error as measured by the three stator segments.

lead to synchronization problems during the switching between subsequent stator segments as will be explained in the next section.

2.2 Problem analysis

Currently, the performance of the system, as controlled by the Bosch-Rexroth NYCe 4000 motion control system, and using Hall-sensors for position sensing is in need of improvement. Figure 2.4 shows the position error for a certain trajectory of the translator (maximum velocity equal to 0.1 m/s, maximum acceleration equal to 1 m/s^2). The figure shows that the position error is very large (maximum of 2.1 mm) and that the measurement of the position error differs between two stator segments. This difference results in a difference in the control action of the two stator segments as verified in Figure 2.5, which shows the force which is exerted on the translator. The figure shows that during the switching interval, both of the stator segments pull (in opposite direction) on the translator, which results in an increase of the force ripple and a decrease of the position accuracy and efficiency.

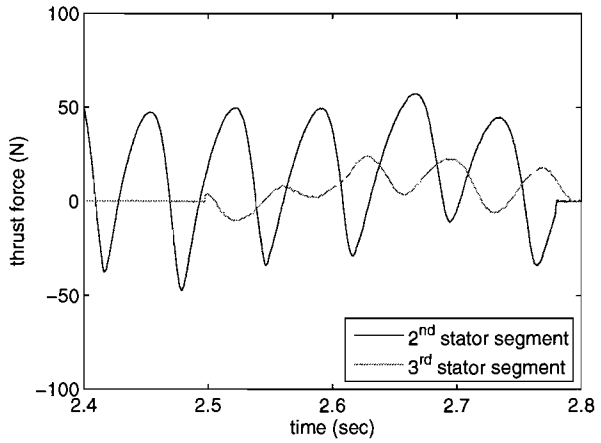

Figure 2.5: Force ripple during the switching interval between the second and third stator segment.

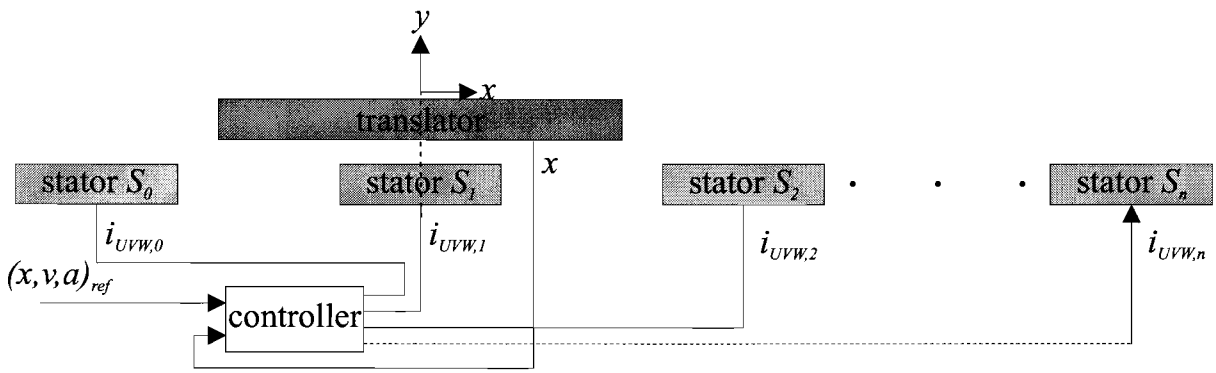

Figure 2.6: For this research proposed global controller structure.

2.3 System adjustments

The goal is to analyze the problems with a physical cause. To be able to focus on these phenomena, the disturbances caused by the control structure are eliminated by changing the control structure. Instead of the "local" control structure which is currently used at Bosch-Rexroth, a control structure with one "global" controller is implemented. Such a "global" controller structure is shown in Figure 2.6. The vector $(x, v, a)_{ref}$ contains the trajectory setpoints and $i_{UVW,n}$ are the setpoints of the (U, V, W)-components of the three-phase current for stator segment n. Also, a linear encoder is used for the position measurement (rather than Hall-sensors), to gain a better accuracy.

2.4 Conclusions

The system as it is currently under development at Bosch-Rexroth experiences significantly large position error and force ripples due to the switching between stator segments. These

problems are partly due to the system structure and partly due to the physical phenomena behind the system. Since the project focuses on the problems with a physical cause, the system is adjusted. To be specific, the "local" control structure is changed to a "global" control structure and the position is measured using a linear encoder rather than Hall-sensors. With these changes, we can focus on the physical phenomena and this is done by an electromagnetic analysis of one actuator segments consisting of one translator and one stator.

Chapter 3

Electromagnetic Analysis of one Actuator Segment

To gain more insight into the electromechanical behaviour of the system, an analysis is made of one segment of the structure, consisting of one translator and one stator segment. The theory behind the linear synchronous motor will be explained starting from the Maxwell equations, and the system is analyzed (in 2D and 3D) using finite element method (FEM) software (Cedrat FLUX v10.1.1) and the simulations are verified from measurements.

3.1 Linear synchronous motor theory

A linear synchronous motor is a motor in which mechanical (linear) motion of the translator is in synchronism with the magnetic field caused by the current through the coils in the stator. Usually, the traveling magnetic field is produced by a three-phase current in the star-connected windings.

Starting with the Maxwell equations in integral form, the principle of a linear synchronous motor can be explained:

$$\text{Ampère's circuital law:} \quad \oint_c \vec{H} \cdot d\vec{l} = \int_S \left(\vec{J} + \frac{\partial \vec{D}}{\partial t} \right) \cdot d\vec{s}, \tag{3.1}$$

$$\text{Gauss' law for magnetism:} \quad \int_S \vec{B} \cdot d\vec{s} = 0, \tag{3.2}$$

$$\text{Faraday's law of induction:} \quad \oint_c \vec{E} \cdot d\vec{l} = -\int_S \frac{\partial \vec{B}}{\partial t} \cdot d\vec{s}, \tag{3.3}$$

$$\text{Gauss' law:} \quad \int_S \vec{D} \cdot d\vec{s} = \int_V \rho dv, \tag{3.4}$$

where S is a surface bounded by a contour c, $\vec{H}$ and $\vec{E}$ are the magnetic and electric field intensity respectively, $\vec{D}$ and $\vec{B}$ are the magnetic and electric flux density respectively, ρ is the free charge density and t is time. Assume the system consists of a stator segment and a translator as shown in Figure 2.2. The stator segment consists of three phases with two coils connected in series per phase. Due to the movement of the magnets, a voltage called the electromotive force (EMF) is induced over the coils. This voltage can be calculated using

(3.3). To this end - assuming that the iron in the stator core does not saturate - the magnetic flux density $\vec{B}$ in the iron core of the stator segment is split in four components:

$$\vec{B} = \vec{B}_{ext} + \Sigma_{j\in\{U,V,W\}}\vec{B}_j, \tag{3.5}$$

where $\vec{B}_{ext}$ is the magnetic flux density due to the magnets and $\vec{B}_j$ is the magnetic flux density due to the current in phase $j \in \{U, V, W\}$.

A phase U of the system, consisting of a coil with an inductance L_U and a resistance R_U, together with the magnetic field caused by the PMs (B_{ext}) and by the current in phase $j \in \{U, V, W\}$ ($\vec{B}_j$) is shown in Figure 3.1. Evaluating (3.3) along the circuit yields:

$$\oint_c \vec{E}\cdot d\vec{l} = \oint_c \vec{E}_s \cdot d\vec{l} + \int_c \vec{E}_c \cdot d\vec{l} = -\oint_c \frac{\partial\left(\vec{B}_{ext} + \Sigma_{j\in\{U,V,W\}}\vec{B}_j\right)}{\partial t}\cdot d\vec{s}, \tag{3.6}$$

where $\int_s \vec{E}_s \cdot d\vec{l}$ is the voltage across the coil:

$$\oint_c \vec{E}_s \cdot d\vec{l} \equiv -V_U, \tag{3.7}$$

and $\int_c \vec{E}_c \cdot d\vec{l}$ is the ohmic voltage drop over the coil:

$$\int_c \vec{E}_c \cdot d\vec{l} = \int_c \frac{\vec{J}}{\sigma}\cdot d\vec{l} = i_U R_U, \tag{3.8}$$

where i_U is the current through the circuit and R_U is the ohmic resistance of the coil. Integration of $\vec{B}$ over a surface S yields the flux linkage ψ and since the derivative operation is a linear operation, it can be taken out of the integral. The magnetic flux density $\vec{B}$ is dependent on time and position. Because of the integration, the position dependency of $\vec{B}$ is eliminated and $\vec{B}$ becomes dependent only on time. Hence, the total time derivative is appropriate, analog to the result found in [5, p. 357]. Using these results, (3.6) can be rewritten as:

$$V_U = i_U R_U + \frac{d\psi_{ext,U}}{dt} + \Sigma_{j\in U,V,W}\frac{d\psi_j}{dt}, \tag{3.9}$$

where $\psi_{ext,U}$ is the flux linkage in phase U due to the permanent magnets, and ψ_j is the linked flux due to the current in phase $j \in \{U, V, W\}$. Since the magnetic material was assumed linear, ψ_{ext} is only dependent on the position x of the translator with respect to the stator segment and $\frac{d\psi_{ext,U}}{dt}$ can be written as $\frac{d\psi_{ext,U}}{dx}\frac{dx}{dt}$. Similarly, $\frac{d\psi_j}{dt}$ is dependent only on the current through the coils (for surface mounted PMs) and can be written as $\frac{d\psi_j}{di_j}\frac{di_j}{dt}$. Because of the linearity of the magnetic material, $\frac{d\psi_j}{di_j}$ is constant. Then, for phase U, $\frac{d\psi_U}{di_U}$ is called the self-inductance L_U, and $\frac{d\psi_V}{di_V}$ and $\frac{d\psi_W}{di_W}$ are called the mutual-inductance M_{VU} and M_{WU} respectively. Then, (3.9) becomes:

$$V_U = i_U R_U + \frac{d\psi_{ext,U}}{dx}\frac{dx}{dt} + L_U\frac{di_U}{dt} + M_{VU}\frac{di_V}{dt} + M_{WU}\frac{di_W}{dt}. \tag{3.10}$$

For now, it is assumed that $M_{ba} = M_{ca} = M$ and $\psi_{ext,U}$ is only dependent on x. Since $i_U = i_V + i_W$, (3.10) can be written as:

$$V_U = i_U R_U + \frac{d\psi_{ext,U}}{dx}\frac{dx}{dt} + (L_U + M)\frac{di_U}{dt}. \tag{3.11}$$

$L_U + M$ is now called the synchronous inductance L_{sU} and indexes U and ext are dropped for simplicity, and then the voltage induced in the coil is equal to:

$$V = iR + \frac{d\psi}{dx}\frac{dx}{dt} + L_s\frac{di}{dt}, \tag{3.12}$$

in which the second term, $\frac{d\psi}{dx}\frac{dx}{dt}$, is called the electromotive force (EMF) e:

$$e(x) = \frac{d\psi}{dx}\frac{dx}{dt}, \tag{3.13}$$

which is the voltage induced over the coils due to the movement of the permanent magnets.

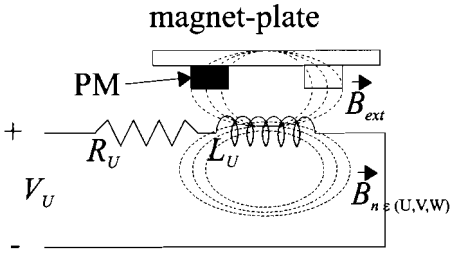

Figure 3.1: Circuit consisting of a resistance R_U and an inductance L_U and a voltage across the leads V_U.

The derivative of the flux linkage with respect to position can be used to find the force exerted on the mover by each phase in the stator. To this end, the total power P in an electromechanical system is given:

$$P = V \cdot i = Ri^2 + \frac{d\psi}{dx}\frac{dx}{dt} \cdot i + \frac{1}{2}L_s\frac{di^2}{dt}, \tag{3.14}$$

in which the term Ri^2 is called the ohmic loss, $\frac{1}{2}L_s\frac{di^2}{dt}$ is the change of energy in the magnetic field caused by the coils and the term $\frac{\partial\psi}{\partial x} \cdot \frac{dx}{dt} \cdot i$ is the mechanical power P_{mech}:

$$P_{mech}(x) = F(x) \cdot \frac{dx}{dt} = \frac{d\psi}{dx} \cdot i(x) \cdot \frac{dx}{dt}, \tag{3.15}$$

such that the force per phase is equal to:

$$F(x) = \frac{d\psi}{dx} \cdot i(x) = k(x) \cdot i(x), \tag{3.16}$$

where $k(x)$ is a force function linking the force $F(x)$ to the current $i(x)$, which, from (3.13), is equal to:

$$k(x) = \frac{d\psi}{dx} = e(x)\left(\frac{dx}{dt}\right)^{-1}. \tag{3.17}$$

In Figure 3.2, a example with one coil and the magnet area is shown, together with the flux linkage and its derivative as function of the position x. For the result shown, the flux linkage as function of position is equal to:

$$\psi(x) = \hat{\psi}\cos\left(\frac{\pi x}{\tau_P}\right), \tag{3.18}$$

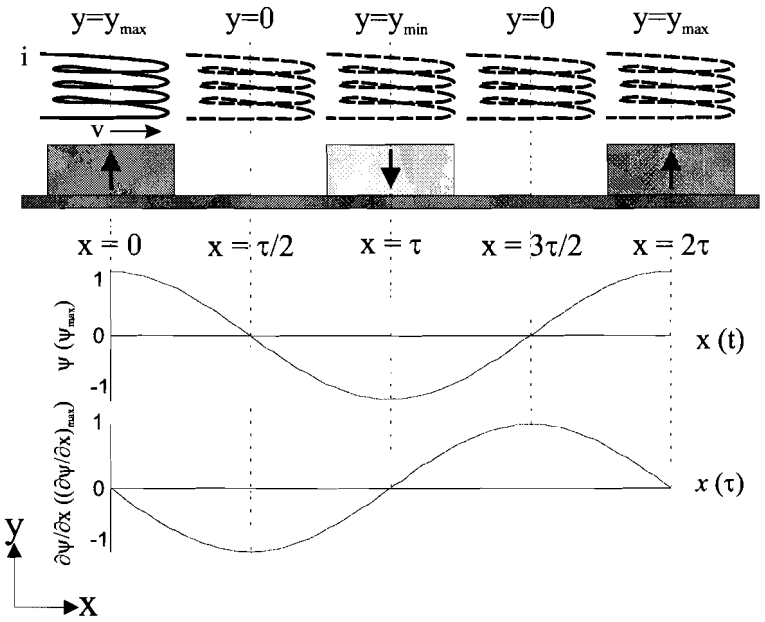

Figure 3.2: Flux linkage and its gradient in a PM linear motor.

its derivative is:

$$\frac{d\psi}{dx} = -\frac{\pi}{\tau_P}\hat{\psi}\sin\left(\frac{\pi}{\tau_P}x\right), \tag{3.19}$$

such that

$$k(x) = -\frac{\pi}{\tau_P}\hat{\psi}\sin\left(\frac{\pi}{\tau_P}x\right). \tag{3.20}$$

For a balanced three-phase system, the force function vector which contains the force function for each phase, is equal to:

$$\vec{k}_{UVW}(x) = \begin{pmatrix} k_U \\ k_V \\ k_W \end{pmatrix}^T = \begin{pmatrix} \hat{k}\sin\left(\frac{\pi x}{\tau_P}\right) \\ \hat{k}\sin\left(\frac{\pi x}{\tau_P} + \frac{4}{3}\pi\right) \\ \hat{k}\sin\left(\frac{\pi x}{\tau_P} + \frac{8}{3}\pi\right) \end{pmatrix}^T, \tag{3.21}$$

with $\hat{k} = -\frac{\pi}{\tau_P}\hat{\psi}$.

3.2 $dq0$-Transformation

To obtain a position independent expression for the force in a (rotating or) linear actuator, the $dq0$-transformation is used [6]. The $dq0$-transformation transforms the stator quantities in a reference frame fixed to the translator. The d-axis (direct axis) and q-axis (quadrature axis) together form a reference frame which is fixed to the translator. In principle, the d-axis is aligned with the translator's permanent magnet flux density and the q-axis is leading the d-axis by 90 electrical degrees. The use of the $dq0$-transformation for a linear synchronous motor can be visualized as shown in Figure 3.3. The stationary frame (U, V, W) is shown as

well as the moving dq-frame moving with a velocity v. For $\theta = 0$, phase U has maximum positive flux linkage from the permanent magnets and the d-axis corresponds with the axis on which the permanent magnets make maximum positive flux. Due to the sinusoidal nature of the flux linkage with respect to the position x, the derivative of the flux linkage is zero at the d-axis and maximum on the q-axis.

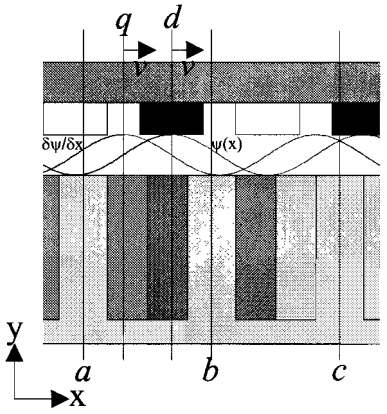

Figure 3.3: Translating dq-frame in the case of a permanent magnet linear synchronous motor. The sinusoidal lines in the airgap represent the magnitude of the flux density caused by the permanent magnet and its derivative.

The $dq0$-transformation matrix $\mathbf{T}$ is used to make a transformation of coordinates from the stationary three-phase coordinate system to the dq rotating coordinate system. This transformation involves two steps. First, the three-phase coordinate system (U_n, V_n, W_n) is projected on the stationary coordinate system $(\alpha_n, \beta_n, 0)$ using:

$$\begin{bmatrix} \alpha_n & \beta_n & 0_n \end{bmatrix} = \frac{2}{3} \begin{bmatrix} 1 & -\frac{1}{2} & -\frac{1}{2} \\ 0 & -\frac{\sqrt{3}}{2} & \frac{\sqrt{3}}{2} \\ \frac{1}{2} & \frac{1}{2} & \frac{1}{2} \end{bmatrix} \begin{bmatrix} U_n \\ V_n \\ W_n \end{bmatrix}. \tag{3.22}$$

Then the projection from $(\alpha_n, \beta_n, 0)$ onto the rotating coordinate system $(d_n, q_n, 0_n)$ is given by:

$$\begin{bmatrix} d_n \\ q_n \\ 0_n \end{bmatrix} = \begin{bmatrix} \cos\theta & \sin\theta & 0 \\ -\sin\theta & \cos\theta & 0 \\ 0 & 0 & 1 \end{bmatrix} \begin{bmatrix} \alpha_n \\ \beta_n \\ 0_n \end{bmatrix} \tag{3.23}$$

Hence, the $dq0$-transformation from the stationary three-phase coordinate system to the rotating $dq0$ coordinate system is equal to:

$$\begin{aligned} \begin{bmatrix} d_n \\ q_n \\ 0_n \end{bmatrix} &= \frac{2}{3} \begin{bmatrix} \cos(\theta) & \cos\left(\theta + \frac{4\pi}{3}\right) & \cos\left(\theta + \frac{8\pi}{3}\right) \\ -\sin(\theta) & -\sin\left(\theta + \frac{4\pi}{3}\right) & -\sin\left(\theta + \frac{8\pi}{3}\right) \\ \frac{1}{2} & \frac{1}{2} & \frac{1}{2} \end{bmatrix} \begin{bmatrix} U_n \\ V_n \\ W_n \end{bmatrix} \\ &= \mathbf{T} \begin{bmatrix} U_n \\ V_n \\ W_n \end{bmatrix}, \end{aligned} \tag{3.24}$$

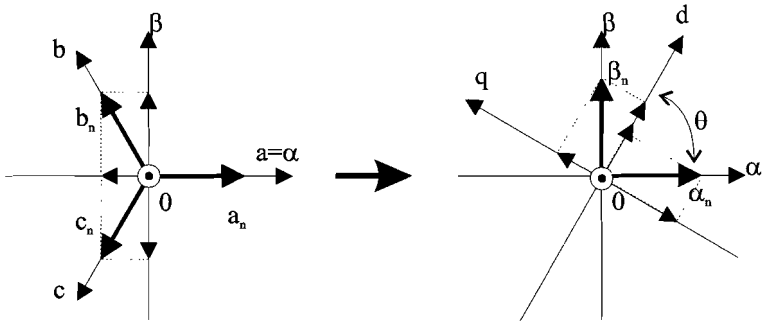

Figure 3.4: $dq0$-transformation.

where $\mathbf{T}$ is the $dq0$-transformation matrix. The steps in the $dq0$-transformation (for rotary machines) are shown in Figure 3.4.

For the linear synchronous motor as shown in Figure 2.2, the transformation matrix $\mathbf{T}$ is equal to:

$$\mathbf{T} = \frac{2}{3}\begin{pmatrix} \cos\left(\frac{\pi x}{\tau}\right) & \cos\left(\frac{\pi x}{\tau}+\frac{4\pi}{3}\right) & \cos\left(\frac{\pi x}{\tau}+\frac{8\pi}{3}\right) \\ -\sin\left(\frac{\pi x}{\tau}\right) & -\sin\left(\frac{\pi x}{\tau}+\frac{4\pi}{3}\right) & -\sin\left(\frac{\pi x}{\tau}+\frac{8\pi}{3}\right) \\ \frac{1}{2} & \frac{1}{2} & \frac{1}{2} \end{pmatrix}, \tag{3.25}$$

In vector notation, the thrust force F_k in the balanced three-phase motor is equal to:

$$F_k = \vec{k}_{UVW} \cdot \vec{i}_{UVW}, \tag{3.26}$$

where $\vec{k}_{UVW}$ and $\vec{i}_{UVW}$ are the (U, V, W)-components of the force function and the current respectively, with $\vec{k}_{UVW}$ equal to:

$$\vec{k}_{UVW} = \begin{pmatrix} k_U \\ k_V \\ k_W \end{pmatrix}^T = \begin{pmatrix} \hat{k}\sin\left(\frac{\pi x}{\tau_P}\right) \\ \hat{k}\sin\left(\frac{\pi x}{\tau_P}+\frac{4}{3}\pi\right) \\ \hat{k}\sin\left(\frac{\pi x}{\tau_P}+\frac{8}{3}\pi\right) \end{pmatrix}^T, \tag{3.27}$$

as given in 3.21. Using the inverse transformation matrix $\mathbf{T}^{-1}$:

$$\mathbf{T}^{-1} = \begin{pmatrix} \cos\left(\frac{\pi x}{\tau_P}\right) & -\sin\left(\frac{\pi x}{\tau_P}\right) & 1 \\ \cos\left(\frac{\pi x}{\tau_P}+\frac{4\pi}{3}\right) & -\sin\left(\frac{\pi x}{\tau_P}+\frac{4\pi}{3}\right) & 1 \\ \cos\left(\frac{\pi x}{\tau_P}+\frac{8\pi}{3}\right) & -\sin\left(\frac{\pi x}{\tau_P}+\frac{8\pi}{3}\right) & 1 \end{pmatrix}, \tag{3.28}$$

the current components in the dq-frame can be transformed onto the (U, V, W)-frame. This results in a position independent expression for the thrust force (in case of surface mounted permanent magnets):

$$\begin{aligned} F_k &= \vec{k}_{UVW} \cdot \vec{i}_{UVW} \\ &= \vec{k}_{UVW} \cdot \mathbf{T}^{-1} \cdot \vec{i}_{dq0} \\ &= \frac{3}{2}\hat{k} i_q. \end{aligned} \tag{3.29}$$

This shows that the thrust force is caused by the current in the q-axis. Because of this, the NYCe4000 motion controller fixes the current in the d-axis to zero.

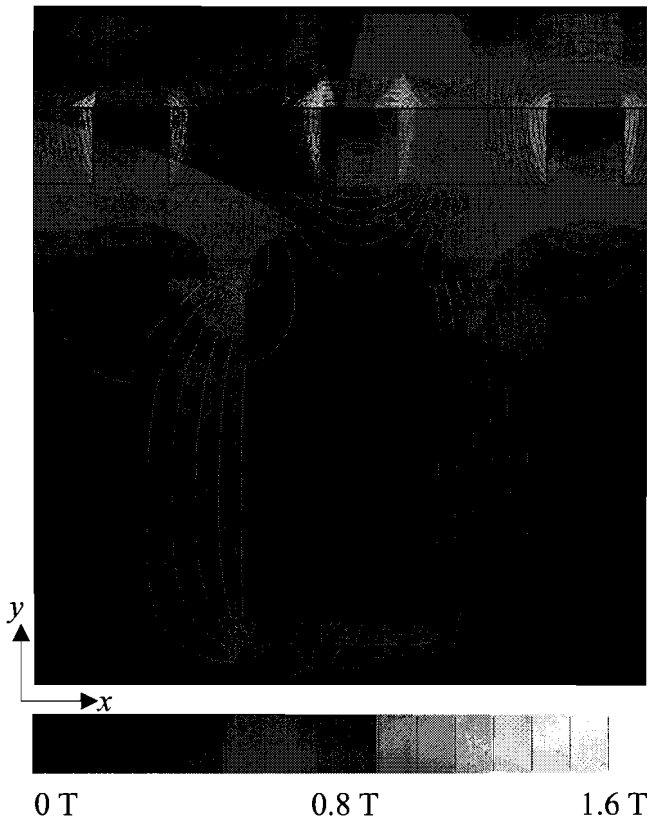

Figure 3.5: Magnitude of the flux density and the flux lines in a detail of the system.

3.3 Magnetic flux density

The assumption was made that the iron cores of the stator segments are magnetically linear. To verify this assumption, the flux density in the iron of the stator segment was calculated (in FEM 2D), in the case that the translator is fully overlapping the stator segment and the currents through the coils are zero. The result is shown in Figure 3.5 and it shows that due to the large airgap, the system experiences significant flux leakage and the flux density in the iron core of the stator does not exceed 0.4 T, which is well below the saturation level of the iron. Because of this, the system can be regarded as magnetically linear, and the inductances in the system can be assumed independent on the current.

It was concluded that there was significant flux leakage: more than half of the flux lines in Figure 3.5 do not (fully) pass through the backiron in the stator, which means that they do not (fully) contribute to the thrust force. This is due to the fact that the airgap is now relatively large compared to the magnet pitch. Due to this large airgap, the flux density in the stator is low and the performance of the linear synchronous motor is decreased (in terms of the force density) with respect to the performance as specified. This will be shown in the next section. Also, due to the low magnetic flux density, the currents in the system will have to increase (compared to a system with an airgap as specified by the manufacturer as shown in Table C.1) to achieve the desired force, resulting in an increase of the losses in the systems. The motor which is chosen for this application is wrong, and a new motor design is desired

to increase performance and efficiency.

3.4 Thrust force

As was shown in (3.20), the force function can be found from the EMF induced over the coils divided by the speed of the translator. Using FEM, the induced EMF is determined and the result of this is shown in Figure 3.6. This shows that, for positions $-0.1 < x < 0.1$, the balanced three-phase voltage has an amplitude of approximately 13.6 V. As the translator moves away from the stator segment, positions $x < -0.1 \wedge x > 0.1$, the EMF which is induced in the coils is no longer a balanced three-phase voltage.

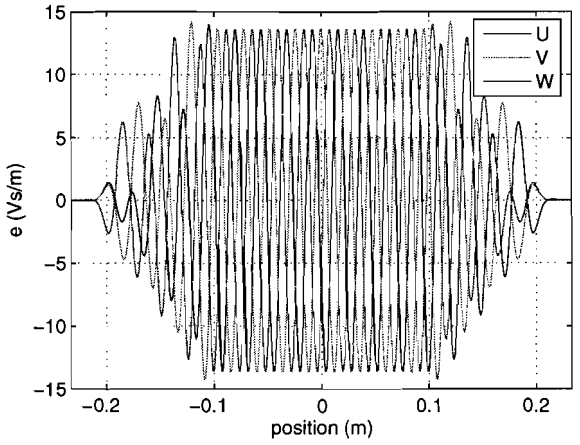

Figure 3.6: EMF for a 5.0 mm airgap obtained from simulation.

The EMF is also measured using a virtual star point, since a connection to the physical star point was not available. Such a configuration is depicted in Figure 3.7. When $R_U = R_V = R_W$, the voltage measured over the resistances R_U, R_V and R_W is then equal to the voltage over the coils L_U, L_V and L_W. The results of these measurements for one stator segment are shown in Figure 3.8. The amplitude of the measured EMF is approximately 14.1 V and the waveforms of the simulation and the measurement show good agreement. For further analysis, the EMF obtained from simulation is used.

In Section 3.2, it was concluded that the thrust force, F_k is equal to

$$F_k = \frac{3}{2}\hat{k}i_q \tag{3.30}$$

Using a current amplitude of $i_q = 1$ A and the EMF waveforms as obtained from simulation (Figure 3.6), the thrust force acting on the translator is shown in Figure 3.9. Figure 3.9 shows that, as long as a stator is completely under the translator, approximately for positions $-0.1 < x < 0.1$, the thrust force (F_k) is constant and equal to $\frac{3}{2}\hat{k}\hat{i_q}$. Beyond these positions, $x < -0.1 \wedge x > 0.1$, the thrust force decreases nonlinearly (as also discussed in [7]). This is due to the fact that it no longer behaves as a balanced three-phase system for these positions (as was concluded earlier from Figure 3.6), which means that the $dq0$-decomposition is not valid. The figure shows that for a current amplitude of 1 A, the force is equal to 20.5 N,

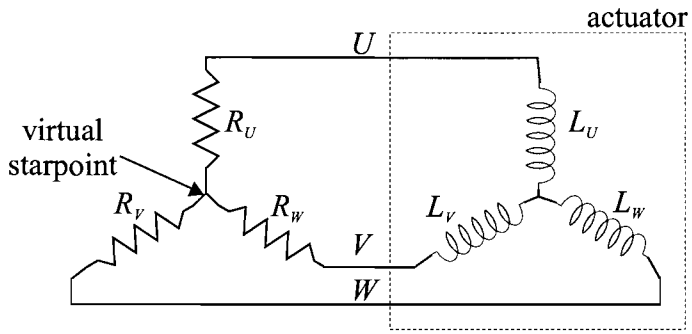

Figure 3.7: Virtual star point configuration.

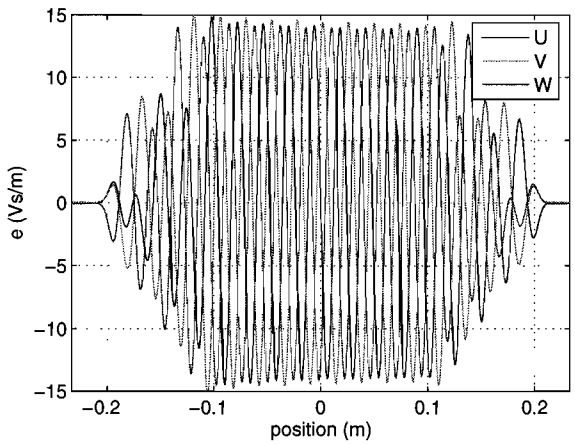

Figure 3.8: EMF for a 5.0 mm airgap obtained from measurement.

which is a significant decrease compared with the value of 93 N as given in the specifications in Appendix B. This is due to the low flux density in the airgap, as was mentioned in the previous section. The ripple in the thrust force for positions $-0.1 < x < 0.1$ is due to the higher harmonics in the EMF-waveforms.

3.5 Cogging force components

The cogging force is a force due to the interactions between the magnets and the backiron in the stator segments. It can be expressed in a formula as:

$$F_{cog}(x) = -\left.\frac{dW_m}{dx}\right|_{i_n=0, n\in\{U,V,W\}}, \tag{3.31}$$

where W_m is the magnetic energy of the system. From FEM (both 2D and 3D, since the skewing of the magnets can not be modeled in 2D), the cogging forces and the end-effects which the translator experiences while moving past a stator segment is obtained and the result is shown in Figure 3.10. For verification, the cogging force is also measured with a

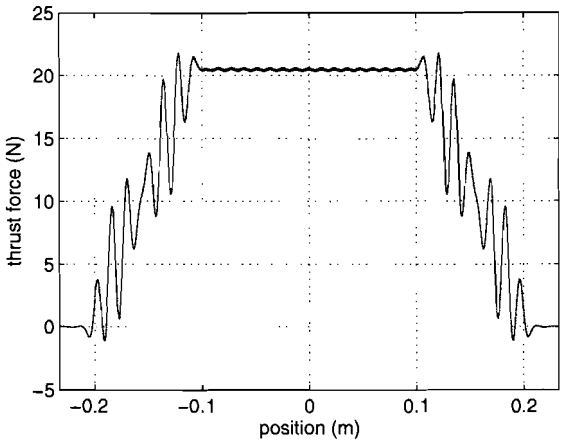

Figure 3.9: Profile of the thrust force acting on the translator with respect to position x obtained from simulation.

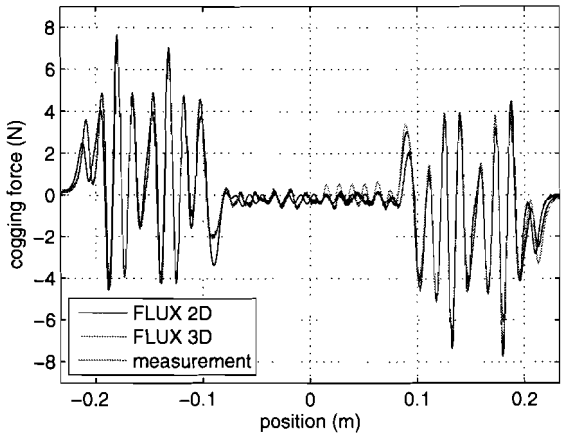

Figure 3.10: Cogging forces acting on the translator obtained from FEM (2D and 3D) and measurements.

load cell. The results show good agreement, which means that skewing of the PMs does not significantly reduce the cogging force in this system. This is due to the fact that the airgap is larger than the system was designed for.

Figure 3.10 shows two different situations. A situation for position $-0.075 < x < 0.075$, where the cogging force is relatively small and is due to the slotted structure and the finite stator length, as is shown in Figure 3.11. Another situation occurs for positions $x < -0.075 \wedge x > 0.075$ where the cogging force is significantly larger and dominated by a cogging force component due to the finite translator length as shown in Figure 3.12. The force ripple due to slotting and the finite stator length has a period of 12 mm (equal to τ_p) and the (fundamental frequency of the) force ripple due to the finite translator length has a period of 16 mm (equal to τ_s). The results from 2D FEM simulations are used during implementation for cogging

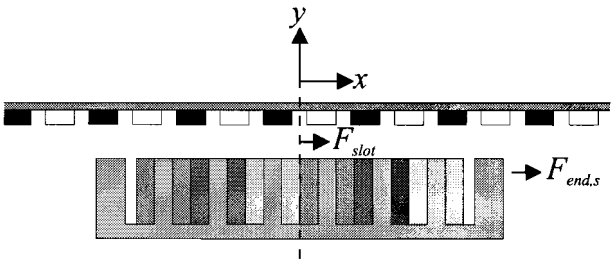

Figure 3.11: Schematic representation of the cogging force components due to slotting and the finite stator length, F_{slot} is the cogging force due to slotting and $F_{end,s}$ is the end-effect due to finite stator length.

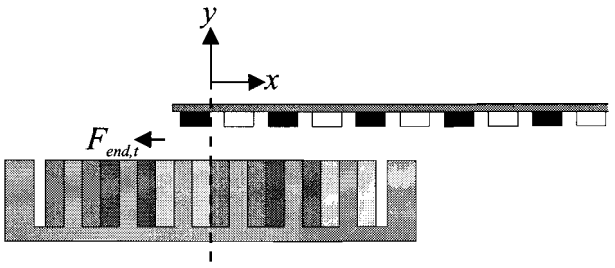

Figure 3.12: Schematic representation of the cogging force component due to the finite translator length, $F_{end,t}$ is the end-effect due to the fact that the translator has a finite length and it is partially overlapping the stator segments when switching between subsequent stator segments

feedforward in Chapter 4.

Using the load cell, the attraction between the iron in the stator segment and the permanent magnets is also measured and compared with the results as found from simulation in Figure 3.13. The figure shows that, when the translator is directly over the stator segment (positions $-0.075 < x < 0.075$), the attraction force is not constant, it is decreasing for increasing x. This indicates that the stator segment and the translator are not parallel, which is due to mounting tolerances of the load cell. This also means that the measurements of the cogging force is distorted. However, these measurements are only used for verification of the simulations. The attraction force has a maximum of approximately 78 N, which is much lower than the specified value as given in Table C.1.

3.6 Reluctance force

The reluctance force, denoted by F_r, is the force caused by a change in inductance of the coils due to the presence of the backiron in the translator. This change in inductance is caused by a change of the reluctance in the airgap. Since the permanent magnets are surface mounted, the reluctance force is zero when the translator is directly over the stator segment. However, due to the finite translator length, the reluctance force which the translator experiences as it moves onto or off the stator segment needs to be verified. The reluctance force can be found

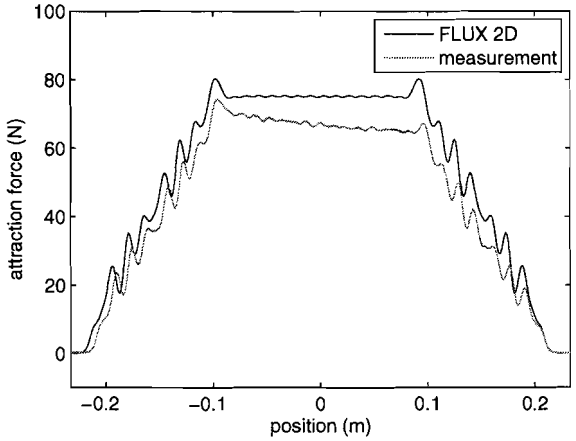

Figure 3.13: Attraction force between stator segment and translator obtained from measurements.

from

$$F_r(x) = \frac{1}{2}\frac{dL}{dx}i^2 \tag{3.32}$$

The self-inductance of the coils as function of the position of the translator above the stator segment has been obtained from simulation (for phase U and W) and is shown in Figure 3.16. The self-inductance increases as the translator moves onto the stator segment. This causes a reluctance force as shown in Figure 3.15. The reluctance force is neglected in the further analysis because of the relatively small amplitude of this force component (max. 0.07 N for $i_U = 1$ A and $i_V = i_W =$ -0.5 A). The simulated value of the self-inductance differs significantly (approximately 15%) from the measured values shown in Table 3.1, however, for the reluctance force only the derivative with respect to position x is of importance. The differences are due to the fact that the simulations are performed in 2D, which does not take the effect of the end-windings into account.

Also, the impedance of the coils in the stator segment as function of the frequency is determined. This is measured using a signal generator and a scope. The result of the measurement is shown in Figure 3.16.

The effect of the presence of the (iron part of the) translator is also obtained from measurements. Several measurements have been made for each of the line-to-line terminals, and the results for the self-inductance in each phase are shown in Table 3.1, together with the results as found from simulation. Table 3.1 shows that the presence of the translator has little influence on the self-inductance of the coils. Also, Table 3.1 shows that the self-inductance of the coils in phase V of the system are significantly larger than the self-inductances in phase U and W. This is due to the physical layout of the phases in the stator segment.

3.7 Conclusions

An electromagnetic analysis of one actuator segment consisting of a translator and a stator is presented. The flux density in the airgap and the iron part of the stator is very low. This causes a significant decrease in the performance of the system with respect to the specifications

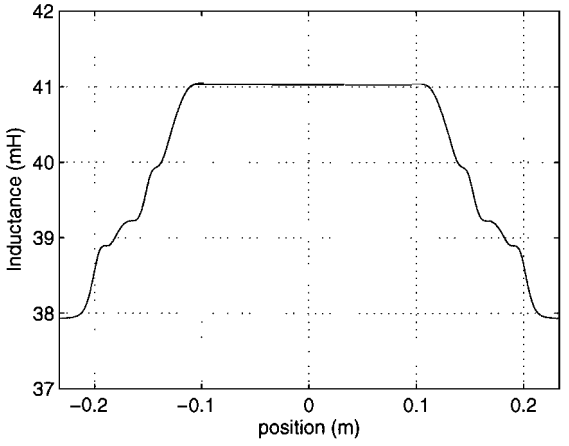

Figure 3.14: Self-inductance of the coils in phase U and W as function of the position of the translator.

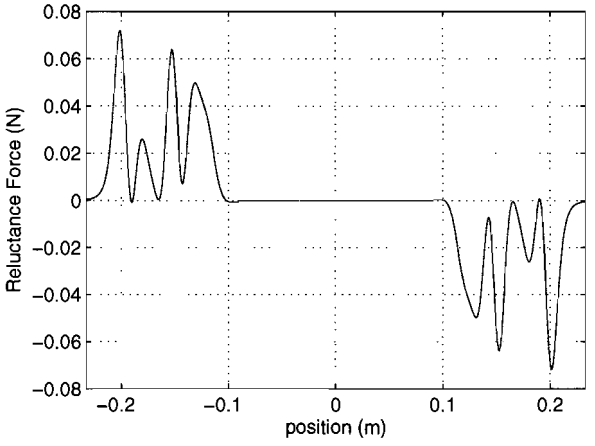

Figure 3.15: Reluctance force due to the a change in inductance of the self-inductances in phase U or W.

Table 3.1: Inductance values obtained from measurements

		measurement	FLUX2D
no translator	L_U	44.1 mH	37.9 mH
	L_V	52.3 mH	46.2 mH
	L_W	44.0 mH	37.9 mH
g = 5.0 mm	L_U	45.0 mH	41.0 mH
	L_V	52.4 mH	46.9 mH
	L_W	45.1 mH	41.0 mH

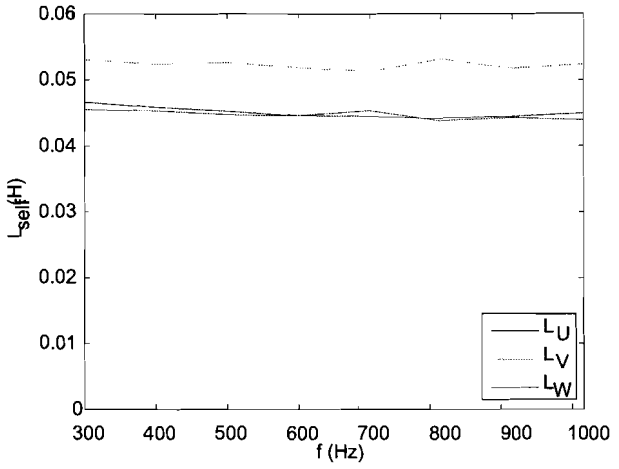

Figure 3.16: Self-inductance of the coils as function of the frequency obtained from measurements.

as supplied by Tecnotion. This is due to the increased airgap. A new design is needed to improve the efficiency of the system. Because of the low flux density value, the system is magnetically linear.

The EMF which is induced in the coils due to the movement of the magnets is a balanced three-phase voltage as long as the translator fully overlaps a stator segment. When the translator only partly overlaps a stator segments, the EMF becomes an unbalanced three-phase voltage. This results in significant ripples in the thrust force when using the $dq0$-transformation to determine the three-phase current.

The cogging force exerted on the translator as it moves over the track is split into three components, namely, the cogging force due to slotting (F_{slot}), the cogging force due to finite stator length ($F_{end,s}$) and the cogging force due to finite translator length ($F_{end,t}$). The end-effect due to the finite translator length is significantly larger than the cogging force due to slotting and the finite stator length. The reluctance force is negligible.

Next, the commutation algorithm, which calculates the three-phase currents in two subsequent stator segments, is studied in more detail. Specifically, the switching interval between two stator segments is investigated.

Chapter 4

Commutation Algorithm

4.1 Controller structure

The controller is a part of the control structure as presented in Figure 2.6. The controller will consist of a feedback controller and feed forward for mass, damping and the cogging force values obtained from measurements and a commutation algorithm which calculates the three-phase current setpoints. Such a controller structure is shown in Figure 4.1, where the values x_{ref}, v_{ref} and a_{ref} are the position, velocity and acceleration setpoint from the trajectory generator and F_{ref} is the desired force setpoint. This chapter focuses on the cogging feedforward and the commutation algorithm which calculates $\vec{i}_{UVW,1,2}$, which are the current vectors $\vec{i}_{UVW}$ for the stator segments S_1 and S_2, based on a desired force $\vec{F}_{ref}$.

4.2 Commutation using $dq0$-based switching algorithms

In Section 3.2, it was concluded that the thrust force, F_k is equal to

$$F_k = \frac{3}{2}\hat{k}i_q \tag{4.1}$$

which shows that the total thrust force is equal to a constant times the current in the q-axis. This means that the commutation algorithm can schematically be represented as shown in

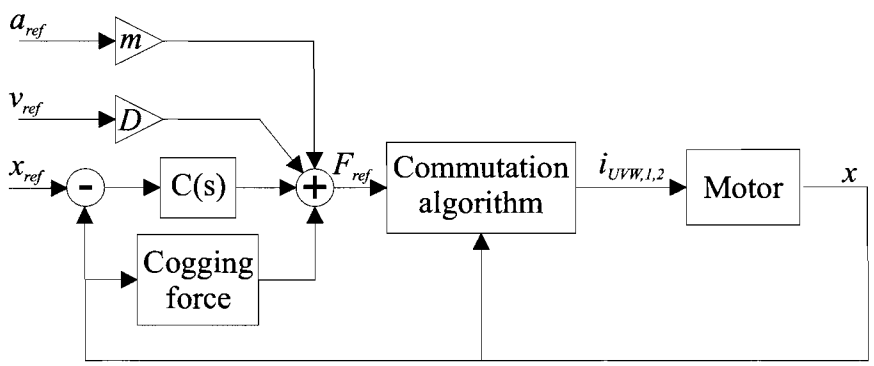

Figure 4.1: Controller structure where m and D are the mass and damping respectively and $C(s)$ is the feedback controller.

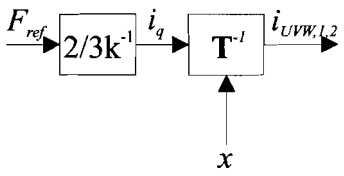

Figure 4.2: Schematic representation of the $dq0$-based commutation algorithm

Figure 4.2. From (4.1), the q-axis current is easily obtained and the three-phase currents in the (U, V, W)-frame are equal to:

$$\begin{pmatrix} i_U \\ i_V \\ i_W \end{pmatrix} = \mathbf{T}^{-1} \cdot \vec{i}_{dq0} = \begin{pmatrix} i_q \sin\left(\frac{\pi x}{\tau_P}\right) \\ i_q \sin\left(\frac{\pi x}{\tau_P} + \frac{4}{3}\pi\right) \\ i_q \sin\left(\frac{\pi x}{\tau_P} + \frac{8}{3}\pi\right) \end{pmatrix}. \tag{4.2}$$

The thrust force due to one stator segment was presented in Figure 3.9. Now, the situation with two stator segments, S_1 and S_2, is considered. Then for a distance d between the two stator segments, the transformation matrix $\mathbf{T}_{12}$ as given earlier in (3.25) becomes:

$$\mathbf{T}_{12} = \frac{2}{3} \begin{pmatrix} \cos\left(\frac{\pi x}{\tau_P}\right) & -\sin\left(\frac{\pi x}{\tau_P}\right) & \frac{1}{2} & 0 & 0 & 0 \\ \cos\left(\frac{\pi x}{\tau_P} + \frac{4\pi}{3}\right) & -\sin\left(\frac{\pi x}{\tau_P} + \frac{4\pi}{3}\right) & \frac{1}{2} & 0 & 0 & 0 \\ \cos\left(\frac{\pi x}{\tau_P} + \frac{8\pi}{3}\right) & -\sin\left(\frac{\pi x}{\tau_P} + \frac{8\pi}{3}\right) & \frac{1}{2} & 0 & 0 & 0 \\ 0 & 0 & 0 & \cos\left(\frac{\pi(x-d)}{\tau_P}\right) & -\sin\left(\frac{\pi(x-d)}{\tau_P}\right) & \frac{1}{2} \\ 0 & 0 & 0 & \cos\left(\frac{\pi(x-d)}{\tau_P} + \frac{4\pi}{3}\right) & -\sin\left(\frac{\pi(x-d)}{\tau_P} + \frac{4\pi}{3}\right) & \frac{1}{2} \\ 0 & 0 & 0 & \cos\left(\frac{\pi(x-d)}{\tau_P} + \frac{8\pi}{3}\right) & -\sin\left(\frac{\pi(x-d)}{\tau_P} + \frac{8\pi}{3}\right) & \frac{1}{2} \end{pmatrix}^T, \tag{4.3}$$

and the inverse $\mathbf{T}_{12}^{-1}$, given in (3.28), is then equal to:

$$\mathbf{T}_{12}^{-1} = \begin{pmatrix} \cos\left(\frac{\pi x}{\tau_P}\right) & -\sin\left(\frac{\pi x}{\tau_P}\right) & 1 & 0 & 0 & 0 \\ \cos\left(\frac{\pi x}{\tau_P} + \frac{4\pi}{3}\right) & -\sin\left(\frac{\pi x}{\tau_P} + \frac{4\pi}{3}\right) & 1 & 0 & 0 & 0 \\ \cos\left(\frac{\pi x}{\tau_P} + \frac{8\pi}{3}\right) & -\sin\left(\frac{\pi x}{\tau_P} + \frac{8\pi}{3}\right) & 1 & 0 & 0 & 0 \\ 0 & 0 & 0 & \cos\left(\frac{\pi(x-d)}{\tau_P}\right) & -\sin\left(\frac{\pi(x-d)}{\tau_P}\right) & 1 \\ 0 & 0 & 0 & \cos\left(\frac{\pi(x-d)}{\tau_P} + \frac{4\pi}{3}\right) & -\sin\left(\frac{\pi(x-d)}{\tau_P} + \frac{4\pi}{3}\right) & 1 \\ 0 & 0 & 0 & \cos\left(\frac{\pi(x-d)}{\tau_P} + \frac{8\pi}{3}\right) & -\sin\left(\frac{\pi(x-d)}{\tau_P} + \frac{8\pi}{3}\right) & 1 \end{pmatrix}. \tag{4.4}$$

Assuming the vectors $\vec{k}_{UVW,12}(x)$ and $\vec{i}_{UVW,12}(x)$ contain the force function of the two stator segments and the current waveforms of the two stator segments respectively, and are given

by:

$$\begin{aligned}\vec{k}(x) &= \begin{pmatrix} k_{S_1U}(x) & k_{S_1V}(x) & k_{S_1W}(x) & k_{S_2U}(x) & k_{S_2V}(x) & k_{S_2W} \end{pmatrix} \\ &= \begin{pmatrix} \hat{k}_{S_1}\sin\left(\frac{\pi x}{\tau_P}\right) \\ \hat{k}_{S_1}\sin\left(\frac{\pi x}{\tau_P}+\frac{4}{3}\pi\right) \\ \hat{k}_{S_1}\sin\left(\frac{\pi x}{\tau_P}+\frac{8}{3}\pi\right) \\ \hat{k}_{S_2}\sin\left(\frac{\pi(x-d)}{\tau_P}\right) \\ \hat{k}_{S_2}\sin\left(\frac{\pi(x-d)}{\tau_P}+\frac{4}{3}\pi\right) \\ \hat{k}_{S_2}\sin\left(\frac{\pi(x-d)}{\tau_P}+\frac{8}{3}\pi\right) \end{pmatrix}^T, \end{aligned} \tag{4.5}$$

and

$$\vec{i}(x) = \begin{pmatrix} i_{U,S_1}(x) \\ i_{V,S_1}(x) \\ i_{W,S_1}(x) \\ i_{U,S_2}(x) \\ i_{V,S_2}(x) \\ i_{W,S_2}(x) \end{pmatrix} \tag{4.6}$$

respectively. Then, as shown in (4.1), the thrust force is the dot-product of $\vec{k}_{UVW,12}(x)$ and $\vec{i}_{UVW,12}(x)$:

$$F_{k,12} = \vec{k}_{UVW,12}(x) \cdot \vec{i}_{UVW,12}(x). \tag{4.7}$$

Using

$$\vec{i}_{dq0,12} = \begin{pmatrix} i_{d,S_1} \\ i_{q,S_1} \\ i_{0,S_1} \\ i_{d,S_2} \\ i_{q,S_2} \\ i_{0,S_2} \end{pmatrix} = \mathbf{T_{12}}^{-1} \cdot \vec{i}_{UVW,12}(x), \tag{4.8}$$

(4.7) can be written as:

$$\begin{aligned} F_{k,12} &= \vec{k}_{UVW,12}(x) \cdot \mathbf{T_{12}}^{-1} \cdot \vec{i}_{UVW,12}(x) \\ &= \frac{3}{2}\left(\hat{k}_{S1} i_{q,S_1} + \hat{k}_{S2} i_{q,S_2}\right), \end{aligned} \tag{4.9}$$

which shows that the currents in the d-axis does not contribute to the thrust force, and can be equal to zero. Then, the (U,V,W)-components for the two stator segments follow from

the dot-product of $\vec{i}_{dq0,12}$ and $\mathbf{T}_{12}^{-1}$:

$$\vec{i}(x) = \begin{pmatrix} i_{U,S_1}(x) \\ i_{V,S_1}(x) \\ i_{W,S_1}(x) \\ i_{U,S_2}(x) \\ i_{V,S_2}(x) \\ i_{W,S_2}(x) \end{pmatrix} = \vec{i}_{dq0,12} \cdot \mathbf{T}_{12}^{-1} \tag{4.10}$$

$$= \begin{pmatrix} 0 \\ i_{q,S_1}(x) \\ 0 \\ 0 \\ i_{q,S_2} \\ 0 \end{pmatrix} \cdot \mathbf{T}_{12}^{-1} \tag{4.11}$$

$$= \begin{pmatrix} i_{q,S_1} \sin\left(\frac{\pi x}{\tau_P}\right) \\ i_{q,S_1} \sin\left(\frac{\pi x}{\tau_P} + \frac{4}{3}\pi\right) \\ i_{q,S_1} \sin\left(\frac{\pi x}{\tau_P} + \frac{8}{3}\pi\right) \\ i_{q,S_2} \sin\left(\frac{\pi(x-d)}{\tau_P}\right) \\ i_{q,S_2} \sin\left(\frac{\pi(x-d)}{\tau_P} + \frac{4}{3}\pi\right) \\ i_{q,S_2} \sin\left(\frac{\pi(x-d)}{\tau_P} + \frac{8}{3}\pi\right) \end{pmatrix}. \tag{4.12}$$

Using the thrust force (F_k) as shown in Figure 3.9 and the cogging force (F_{cog}) shown in Figure 3.10, the total force ($F_k + F_{cog}$) acting on the translator due to the two stator segments can be determined as the sum of these two force profiles and is only dependent on the distance d between the stator segments. Choosing for the distance d the arbitrary value of $d = 0.33$ m, the total force profile is shown in Figure 4.3. There are significant force ripples during the switching interval between the subsequent stator segments, and it is investigated whether there exists an optimal value of d for which the total force ripple is minimized. To this end, the standard deviation of the force profile as function of the distance between subsequent stator segments is determined. The result of this is shown in Figure 4.4, where F_k, F_{cog} and F_{tot} represent the standard deviation of the thrust, cogging and total force profile respectively. The distance for which the standard deviation of the force profile is minimized, is the optimal distance. Figure 4.4 shows that the minima of the standard deviation of the three force profiles coincide, and that the optimal distance between subsequent stators is equal to 312.6 mm (the length of the translator). Figure 4.4 shows that the force ripple is mostly due to the cogging force components. These cogging force components can be compensated by feedforwarding the values known from simulation. Using this optimal distance, the force has the shape as shown in Figure 4.5, in which two situations are compared: one with and one without cogging force feedforward. It shows that the force ripple with cogging force feedforward is still significant, being approximately 10% of the thrust force for an amplitude of the current of 1 A. For comparison, Figure 4.6 shows the switching between subsequent stator segments at a (nonoptimal) distance of $d = 0.33$ m apart, also with and without cogging feedforward. It can be concluded that in this case, the two results do not differ significantly. This is partly due to the fact that the force ripple in the thrust force increases significantly when the value of

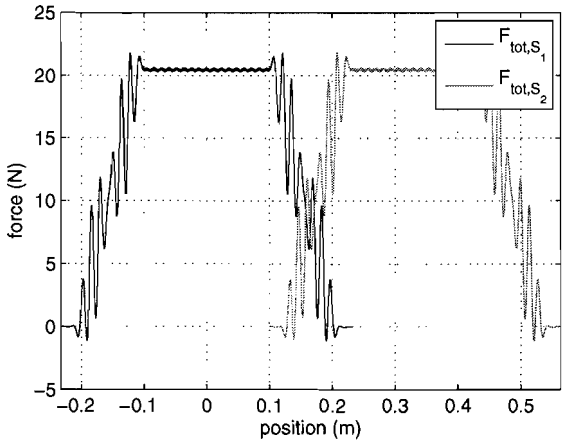

Figure 4.3: Force profiles for subsequent stators S_1 and S_2 at a distance $d = 0.33$ m apart, where F_{tot,S_i} is the total force due to stator $i \in \{S_1, S_2\}$ using the $dq0$-based commutation algorithm

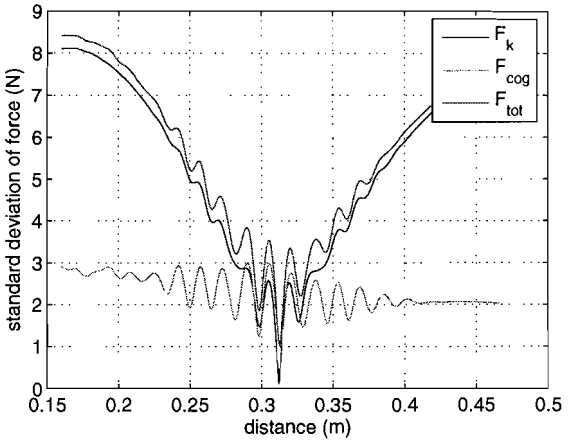

Figure 4.4: Standard deviation of force for various distances between subsequent stators using the $dq0$-based commutation algorithm, where F_{tot} is the total force, F_k is the force due to the current in the windings and F_{cog} is the cogging force and end-effects. The optimal distance is found to be 312.6 mm.

d is not the optimal value of 0.3126 m. On top of this, the cogging feedforward does not work properly anymore, since the performance of this feedforward is dependent on the accuracy of the thrust force.

4.3 direct force-current decoupling commutation algorithm

As shown in the previous section, the system under study is not a balanced three-phase system for the entire stroke of the translator. Because of this the $dq0$-transformation to calculate the

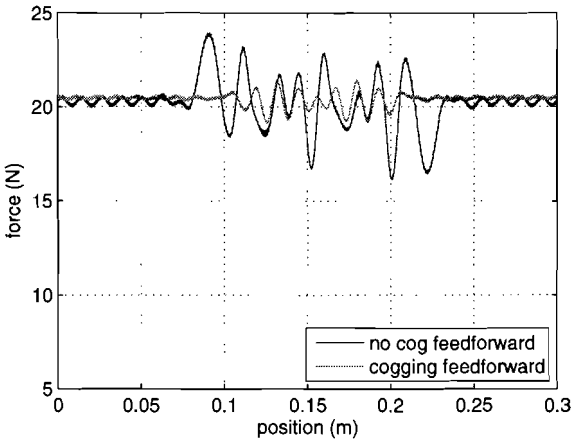

Figure 4.5: Profile of the total force acting on the translator during commutation between subsequent stators at the optimal distance of 312.6 mm apart using the $dq0$-based commutation algorithm.

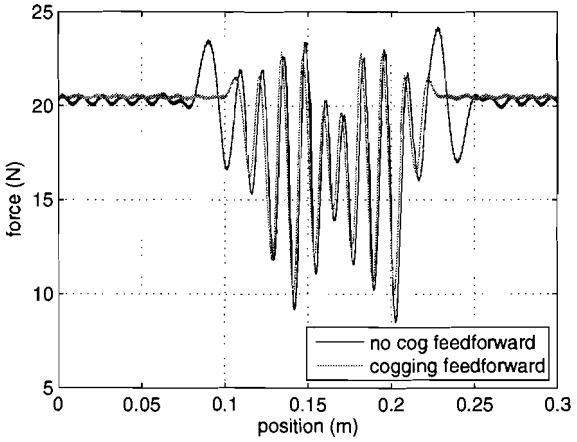

Figure 4.6: Profile of the total force acting on the translator during commutation between subsequent stators at the nonoptimal distance of 330 mm apart using the $dq0$-based commutation algorithm.

three-phase current is incorrect and using a $dq0$-based switching algorithm results in force ripples. Therefore, the current per phase is calculated based on the instantaneous value of the EMF per phase.

A situation with two stator segment segments, S_1 and S_2, and one translator is considered. Two vectors, $\vec{i}(x)$ and $\vec{k}(x)$, contain the current through each phase of the two stator segments and the force function per phase of the two stator segments respectively:

$$\vec{i}(x) = \begin{pmatrix} i_{S_1U}(x) \\ i_{S_1V}(x) \\ i_{S_1W}(x) \\ i_{S_2U}(x) \\ i_{S_2V}(x) \\ i_{S_2W}(x) \end{pmatrix}; \vec{k}(x) = \begin{pmatrix} k_{S_1U}(x) \\ k_{S_1V}(x) \\ k_{S_1W}(x) \\ k_{S_2U}(x) \\ k_{S_2V}(x) \\ k_{S_2W}(x) \end{pmatrix}^T . \tag{4.13}$$

The thrust force, $F_k(x)$, is equal to:

$$F_k(x) = \vec{k}(x)\,\vec{i}(x). \tag{4.14}$$

Objective is now to find an expression for the current so that the thrust force in the system is equal to a reference force, $\vec{F}_{ref}$ as presented in Figure 4.1, at each position. The expression for $\vec{i}(x)$ is found analog to [8]. Also, since a three-phase amplifier is used and a connection to the neutral point is not available, the sum of the currents through each of the stators has to be zero. To include this last requirement in the equations, (4.14) is written as:

$$\begin{pmatrix} \vec{F}_{ref}(x) \\ 0 \\ 0 \end{pmatrix} = \begin{pmatrix} k_{S_1U}(x) & k_{S_1V}(x) & k_{S_1W}(x) & k_{S_2U}(x) & k_{S_2V}(x) & k_{S_2W} \\ 1 & 1 & 1 & 0 & 0 & 0 \\ 0 & 0 & 0 & 1 & 1 & 1 \end{pmatrix} \begin{pmatrix} i_{S_1U}(x) \\ i_{S_1V}(x) \\ i_{S_1W}(x) \\ i_{S_2U}(x) \\ i_{S_2V}(x) \\ i_{S_2W}(x) \end{pmatrix}$$

$$\vec{F}(x) = \mathbf{k}(x)\,\vec{i}(x). \tag{4.15}$$

For the total system to be controllable, the rank of matrix $\mathbf{k}(x)$ should be equal to the number of degrees-of-freedom, $n = 3$, for all desired values of x which are defined as a set X.

$$\operatorname{rank}(\mathbf{k}(x)) = n, \forall x \in X \subset \mathbb{R}. \tag{4.16}$$

Assuming that (4.16) holds, $\mathbf{k}(x)$ is a consistent mapping. Therefore, and since the system is overactuated (i.e. the number of inputs is greater than the number of degrees-of-freedom), there exists an infinite set of possible solutions for $g(x)$ for the equation:

$$\mathbf{k}(x)\,\mathbf{g}(x) = \mathbf{I}, \forall x \in S. \tag{4.17}$$

A solution is then chosen such that the dissipated power is minimized. This is obtained from the 2-norm optimization criteria:

$$\min_{\vec{F}_k(x)=\mathbf{k}(x)\vec{i}(x)} \|\vec{i}\|_2 = \|\mathbf{k}^-(x)\,\vec{F}(x)\|_2. \tag{4.18}$$

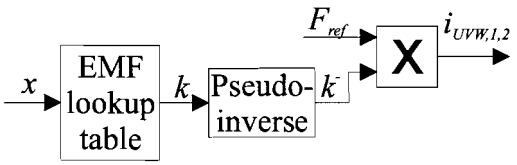

Figure 4.7: Control structure for the system using the switching algorithm based on the instantaneous values of the EMF per phase.

Where $\mathbf{k}^{-}(x)$ is the Moore-Penrose pseudoinverse [9] of $\mathbf{k}(x)$, which is equal to:

$$\mathbf{k}^{-}(x) = \mathbf{k}^{T}(x)\left(\mathbf{k}(x)\,\mathbf{k}^{T}(x)\right)^{-1} \tag{4.19}$$

The currents $\vec{i}$ can then be found with:

$$\vec{i}(x) = \mathbf{k}^{-}(x)\,\vec{F}_{k}(x)\,. \tag{4.20}$$

Schematically, the algorithm, which is called direct force-current decoupling switching algorithm analog to [8], can be represented as shown in Figure 4.7.

To test this disturbance compensation it has been implemented in Simulink. As in the previous chapter, the situation with two stator segments, S_1 and S_2 positioned at a distance d, is considered. The first simulation, shown in Figure 4.8, uses an optimal value of $d = 0.3126$ m for the distance between stator segments, and compares the results with and without cogging feedforward. During the second simulation, shown in Figure 4.9, the distance between subsequent stator segments is equal to the (non-optimal) value of $d = 0.33$ m. The two figures show that in both cases, the force ripple can be reduced to zero. Now, to compare the results between the two commutation algorithms, Figure 4.10 shows the results obtained from simulations for two stator segments at the (non-optimal) distance of $d = 0.33$ m, using the $dq0$-based commutation algorithm (indicated by $F_{tot,dq0}$) and using the direct force-current decoupling commutation algorithm (indicated by $F_{tot,EMF}$). The result differ significantly. In the case of the direct force-current decoupling commutation algorithm, the force ripple is reduced to zero, whereas in the case of the $dq0$-based commutation algorithm, the force ripple is approximately 50% of the thrust force. Comparing Figures 4.8 and 4.9, it is concluded that the direct force-current decoupling switching algorithm makes the performance of the system (in terms of the force ripple) less dependent on the distance d between subsequent stator segments, since in both cases, the force ripple is reduced to zero.

The currents as calculated by the direct force-current decoupling switching algorithm (with cogging feedforward) are shown in Figure 4.11. To investigate the behaviour of the three-phase currents in the stator segments in the case of a balanced three-phase EMF, (4.19) is solved for $\mathbf{k}(x)$ equal to (4.21), where d is the distance between the stator segments, resulting in (4.22). This means that the current $\vec{i}(x)$ is equal to (4.23), where $F_{des}(x)$ is the desired force. Consequently, for a balanced three-phase system, the currents are also balanced three-phase,

which is a similar result as found from (4.10).

$$\mathbf{k}(x) = \begin{pmatrix} \hat{k}_{S_1} \sin\left(\frac{\pi x}{\tau_P}\right) & 1 & 0 \\ \hat{k}_{S_1} \sin\left(\frac{\pi x}{\tau_P} + \frac{4}{3}\pi\right) & 1 & 0 \\ \hat{k}_{S_1} \sin\left(\frac{\pi x}{\tau_P} + \frac{8}{3}\pi\right) & 1 & 0 \\ \hat{k}_{S_2} \sin\left(\frac{\pi(x-d)}{\tau_P}\right) & 0 & 1 \\ \hat{k}_{S_2} \sin\left(\frac{\pi(x-d)}{\tau_P} + \frac{4}{3}\pi\right) & 0 & 1 \\ \hat{k}_{S_2} \sin\left(\frac{\pi(x-d)}{\tau_P} + \frac{8}{3}\pi\right) & 0 & 1 \end{pmatrix}^T \tag{4.21}$$

$$\mathbf{k}^-(x) = \frac{2}{3} \begin{pmatrix} \frac{k_{S_1}}{k_{S_1}^2+k_{S_2}^2} \sin\left(\frac{\pi x}{\tau_P}\right) & \frac{1}{2} & 0 \\ \frac{k_{S_1}}{k_{S_1}^2+k_{S_2}} \sin\left(\frac{\pi x}{\tau_P} + \frac{4}{3}\pi\right) & \frac{1}{2} & 0 \\ \frac{k_{S_1}}{k_{S_1}^2+k_{S_2}^2} \sin\left(\frac{\pi x}{\tau_P} + \frac{8}{3}\pi\right) & \frac{1}{2} & 0 \\ \frac{k_{S_2}}{k_{S_1}^2+k_{S_2}^2} \sin\left(\frac{\pi(x-d)}{\tau_P}\right) & 0 & \frac{1}{2} \\ \frac{k_{S_2}}{k_{S_1}^2+k_{S_2}^2} \sin\left(\frac{\pi(x-d)}{\tau_P} + \frac{4}{3}\pi\right) & 0 & \frac{1}{2} \\ \frac{k_{S_2}}{k_{S_1}^2+k_{S_2}^2} \sin\left(\frac{\pi(x-d)}{\tau_P} + \frac{8}{3}\pi\right) & 0 & \frac{1}{2} \end{pmatrix} \tag{4.22}$$

$$\begin{aligned} \begin{pmatrix} i_{S_1U}(x) \\ i_{S_1V}(x) \\ i_{S_1W}(x) \\ i_{S_2U}(x) \\ i_{S_2V}(x) \\ i_{S_2W}(x) \end{pmatrix} &= \mathbf{k}^-(x) \begin{pmatrix} F_{des}(x) \\ 0 \\ 0 \end{pmatrix} \\ &= \frac{2F_{des}(x)}{3} \begin{pmatrix} \frac{k_{S_1}}{k_{S_1}^2+k_{S_2}^2} \sin\left(\frac{\pi x}{\tau_P}\right) \\ \frac{k_{S_1}}{k_{S_1}^2+k_{S_2}^2} \sin\left(\frac{\pi x}{\tau_P} + \frac{4}{3}\pi\right) \\ \frac{k_{S_1}}{k_{S_1}^2+k_{S_2}^2} \sin\left(\frac{\pi x}{\tau_P} + \frac{8}{3}\pi\right) \\ \frac{k_{S_2}}{k_{S_1}^2+k_{S_2}^2} \sin\left(\frac{\pi(x-d)}{\tau_P}\right) \\ \frac{k_{S_2}}{k_{S_1}^2+k_{S_2}^2} \sin\left(\frac{\pi(x-d)}{\tau_P} + \frac{4}{3}\pi\right) \\ \frac{k_{S_2}}{k_{S_1}^2+k_{S_2}^2} \sin\left(\frac{\pi(x-d)}{\tau_P} + \frac{8}{3}\pi\right) \end{pmatrix}. \end{aligned} \tag{4.23}$$

Figure 4.11 shows that the amplitude of the current increases during the switching interval from S_1 to S_2. The amplitude of the current further increases when the distance d between S_1 and S_2 increases. As stated in Table 2.1, the maximum current which the coils can carry is limited to 6 A. Because of this, the maximum force which can be exerted on the translator over the entire stroke decreases as function of d. This maximum force as function of the distance d is shown in Figure 4.12. The minimum distance is 118 mm (the length of a stator

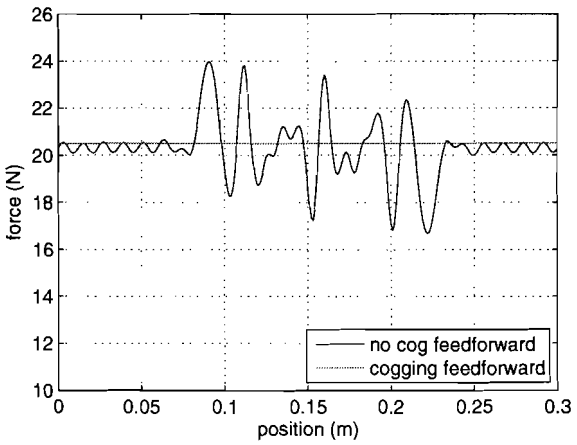

Figure 4.8: Forces during commutation between two stator segments at an (optimal) distance of $d = 0.3126$ m apart obtained from simulation with and without cogging feedforward using the direct force-current decoupling commutation algorithm.

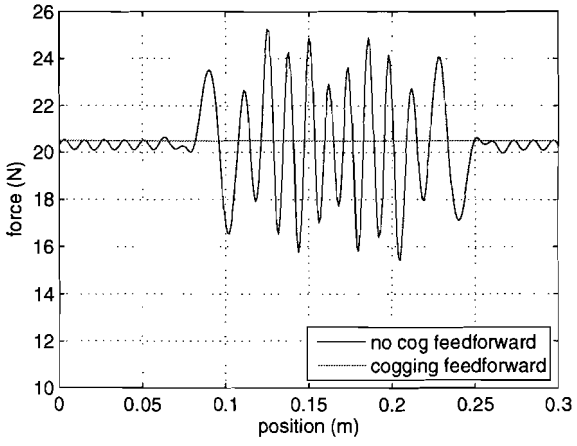

Figure 4.9: Forces during commutation between two stator segments at an (nonoptimal) distance of $d = 0.33$ m apart obtained from simulation with and without cogging feedforward using the direct force-current decoupling commutation algorithm.

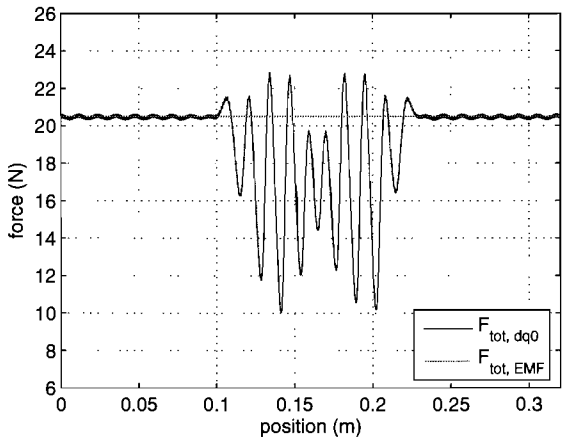

Figure 4.10: Forces during commutation between two stator segments at an (nonoptimal) distance of $d = 0.33$ m apart obtained from simulation with cogging feedforward, where $F_{tot,dq0}$ is the total force when using the $dq0$-based switching algorithm and $F_{tot,EMF}$ is the the total force when using the EMF-based switching algorithm.

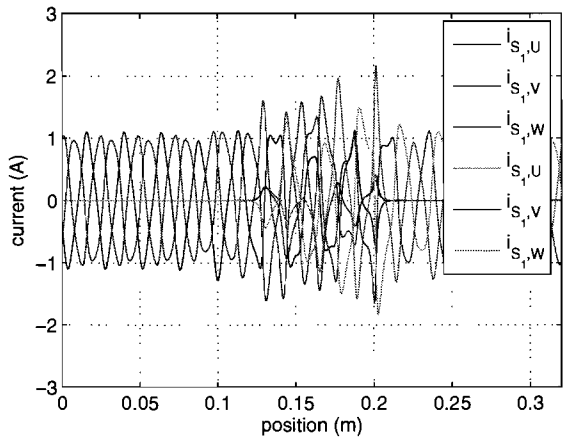

Figure 4.11: Three-phase current through the coils in stators S_1 and S_2 during commutation between these subsequent stator segments obtained from simulation with cogging feedforward. The current values compensate for both the cogging force and end-effects.

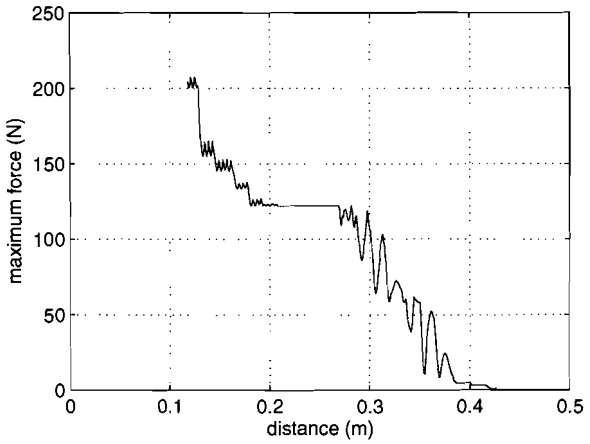

Figure 4.12: The maximum force which can be exerted on the translator over the entire stroke as function of the distance between subsequent stator segments.

segment), which means that the stator segments are placed directly adjacent to each other. For a distance greater than 0.4 m, the distance between the stator segments becomes too large, which means that the thrust force which is exerted on the translator becomes zero. This means that the translator has to move on its kinetic energy and it cannot be controlled (i.e. positioned) between the stator segments.

As was said in Section 3.2, the NYCe4000 controller fixes the current in the d-axis to zero. This would be allowed if the system has a balanced three-phase force function for the entire stroke of the translator. However, this is not the case, so the behaviour of the d and q-axis currents are calculated (using the current values as shown in Figure 4.11) and shown in Figure 4.13. The current in the d-axis is not zero (especially during the switching interval), and, therefore, the NYCe4000 software will have to be adjusted to implement this algorithm.

4.4 Experimental verification

To verify the performance of the new commutation algorithm, it has been implemented on a test track consisting of three stator segments and one translator. A photo of the system is shown in Figure 4.14. There are several differences between the system shown in Figure 2.1. Most notably (as was mentioned earlier), the system now uses a linear encoder for position sensing, rather than the Hall-sensors. Also, the bearing system is different.

The system is controlled using a dSpace CP1103 controller board. The position of the translator is determined with a Heidenhain LIDA 47 linear encoder, with a resolution of 2 μm, and the coils are powered by ELMO FLU-3/100 amplifiers. The maximum voltage is 75 V, limiting the velocity and acceleration to 0.5 m/s resp. 3 m/s^2. The positions of the (midpoints of the) stator segments are shown in table 4.1.

The controller which is used for implementation is the controller shown in Figure 4.1. The

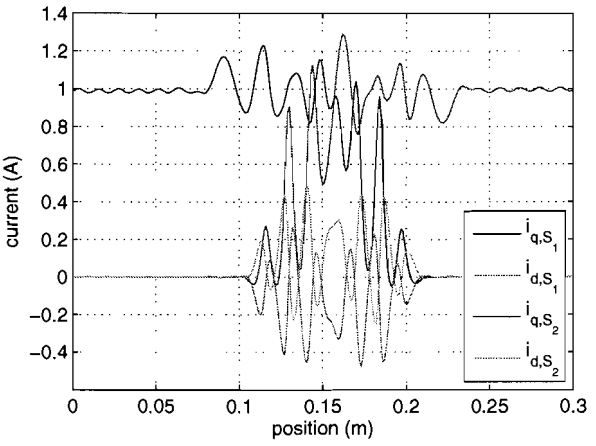

Figure 4.13: dq-Current through the coils in stators S_1 and S_2 during commutation between these subsequent stator segments obtained from simulation with cogging feedforward. The current values compensate for both the cogging force and end-effects.

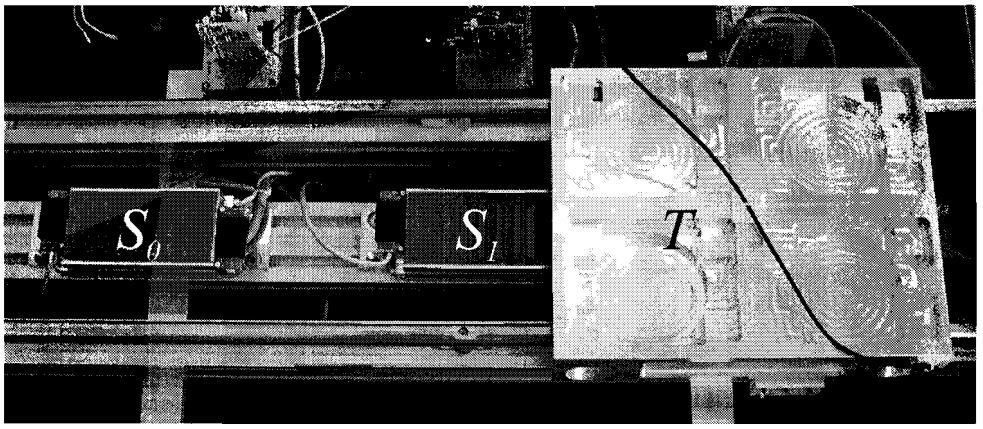

Figure 4.14: Picture of the setup, where S_0 and S_1 are stator segments and T is the translator. Currently, stator segment S_2 is underneath the translator.

Table 4.1: Positions of the stators

stator	position (m)
S_0	0.3126
S_1	0
S_2	-0.33

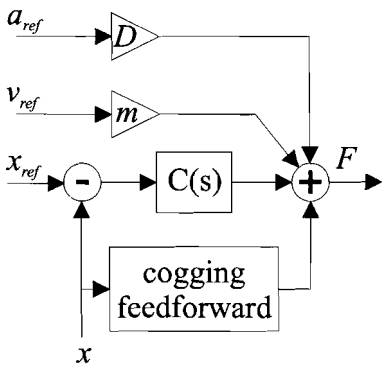

Figure 4.15: Controller used for implementation, with feedforward of mass (m), damping (D) and cogging force.

transfer function $C(s)$ is a PD-controller equal to:

$$C(s) = 57935422.593\frac{s + 20.94}{(s + 377)(s + 188.5)}, \tag{4.24}$$

which is obtained from Appendix A. The magnitude of the frequency response of the closed loop transfer function

$$\frac{P(s)C(s)}{1 + P(s)C(s)}, \tag{4.25}$$

where $P(s)$ is the transfer function of the linear synchronous motor:

$$P(s) = \frac{1}{ms^2 + Ds}, \tag{4.26}$$

where m is the mass of the translator and D is the damping, is shown in Figure 4.16, which shows that the closed loop bandwidth of the system is approximately 18 Hz. For a maximum speed of 0.5 m/s, the cogging force component due to slotting and the finite stator length has a (fundamental) frequency of approximately $f_{slot-end,s} = \frac{0.5}{12 \cdot 10^{-3}} = 41.7$ Hz and the cogging force component due to the finite translator length has a (fundamental) frequency of approximately $f_{slot-end,t} = \frac{0.5}{16 \cdot 10^{-3}} = 31.3$ Hz, which means that the bandwidth of the closed loop system is lower than the main frequencies of the disturbances.

For comparison, both the $dq0$-based switching algorithm, as well as the direct force-current decoupling switching algorithm were implemented. The position error of the translator as function of time is shown in Figure 4.17. The translator moves with a maximum velocity of 0.5 m/s, a maximum acceleration of 2 m/s^2 and a jerk equal to 1000 m/s^3. From these results, it is clear that the direct force-current decoupling switching algorithm performs especially well, compared to the $dq0$ switching algorithm, during the switching interval from stator segment S_1 to stator segment S_2. Apart from this interval, the performance between the two switching algorithms is similar. Since the distance between stator segment S_0 and S_1 is equal to the optimal value of 312.6 mm, the performance during this switching interval should not differ significantly between the two switching algorithms, as can be concluded comparing Figures 4.5 and 4.8. Figure 4.10 shows that for $d = 0.33$ m, the direct force-current decoupling switching algorithm performs better than the $dq0$-based switching algorithm, and the measurements confirm this conclusion. The direct force-current decoupling switching algorithm makes the position error less dependent on the distance between subsequent stator segments.

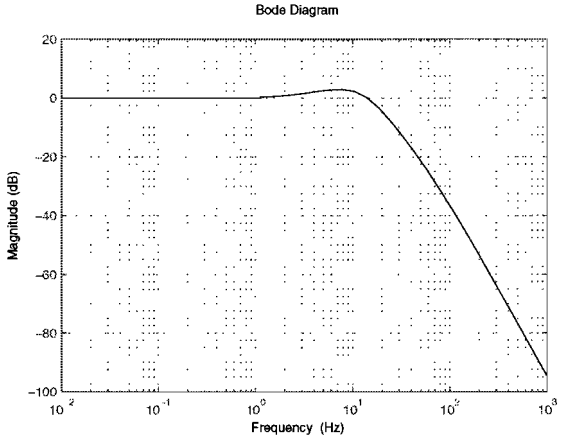

Figure 4.16: Magnitude of the frequency response of the closed loop transfer function.

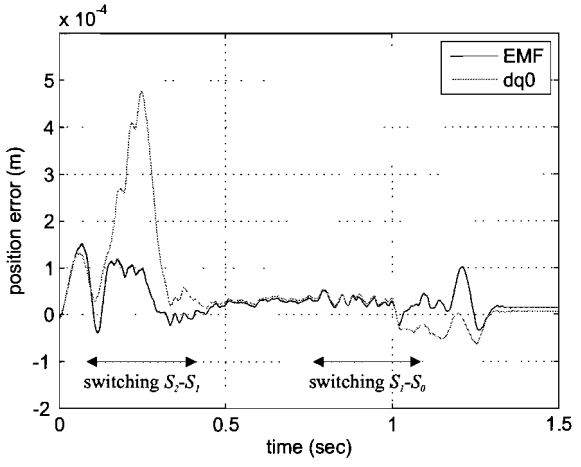

Figure 4.17: Position error as function of time, where EMF indicates the result found using the direct force-current decoupling switching algorithm and $dq0$ indicates the result found using the $dq0$ switching algorithm and switching $S_0 - S_1$ and $S_1 - S_2$ indicates switching interval from stator segment S_0 to S_1 and S_1 to S_2 respectively.

4.5 Conclusions

Both the $dq0$-based algorithm as well as the direct force-current decoupling commutation algorithm have been verified from simulations and implementation in an experimental setup. It was concluded that the $dq0$-based algorithm is not valid for the entire stroke of the translator. When the translator partly overlaps a stator segment, the EMF waveforms which are induced in the coils of the stator segment are not balanced three-phase voltages, which is a requirement for the $dq0$-based algorithm. This causes force-ripples (which are dependent on the distance between the stator segments). To eliminate these force ripples, the direct force-current decoupling commutation algorithm has been implemented which calculates the current setpoints based on the instantaneous EMF values. It is concluded that, when using this algorithm, the current in the d-axis is not equal to zero when the translator switches between stator segments.

Chapter 5

Conclusions and recommendations

5.1 Conclusions

- A thorough electromagnetic analysis of this system identified the following problems:
  - The chosen machine (Tecnotion TL-6N) is not suitable for this airgap size, resulting in a significant reduction of the performance with regards to the specifications.
  - The EMF induced in the system is not a balanced three-phase voltage during the switching interval between subsequent stator segments.
  - The cogging forces which are exerted on the translator during this switching interval are significantly large compared to the situation where the translator is fully overlapping one stator segment.
- The $dq0$-based commutation algorithm is not valid for this system due to the fact that the EMF is not a balanced three-phase voltage for the entire stroke of the translator.
- A novel commutation algorithm, which has been named the direct force-current decoupling commutation algorithm, was investigated and implemented. The new algorithm calculates the current values based on the EMF and significantly improves the dynamic performance:
  - The force ripples can theoretically be reduced to zero, independent on the distance between stator segments.
  - The position error is significantly decreased with respect to the $dq0$-based commutation algorithm.

5.2 Recommendations

- A new electromagnetic design for a linear actuator with a segmented stator is needed. This new design should improve the performance of the system in terms of:
  - Proper balance between the electric and magnetic loading resulting in a decrease in the flux leakage and a higher flux density in the airgap.
  - Reduction of the cogging force during the switching interval between subsequent stator segments.

  - Optimization of the EMF-waveform in such a way that it can be approximated by a linear function, allowing for a simpler control structure (i.e. lookup-tables with the EMF-values are no longer needed).

- The new commutation algorithm can be implemented in the original control structure assuming that the position measurement is synchronized among the stator segments.

Appendix A

Controller parameters

To find a suitable (PD) controller for this system, the loop shaping procedure as presented in [10] was used:

1. Stabilize the plant: lead/lag filter is added:

$$H_{ll}(s) = \frac{3(s + bw/3)}{(s + 3bw)}, \tag{A.1}$$

   where $H_{ll}(s)$ is the transfer function of the lead/lag filter and bw is the bandwidth of the controller.

2. Add low-pass filter:

$$H_{lpf}(s) = \frac{6bw}{s + 6bw}, \tag{A.2}$$

   where $H_{lpf}(s)$ is the transfer function of the low-pass filter .

3. Gain correction:

$$G = mbw^2 + Dbw \tag{A.3}$$

   where G is the gain of the controller, m is the mass of the translator and D is the damping of the system.

Such that the controller is equal to:

$$C(s) = GH_{ll}(s) H_{lpf}(s). \tag{A.4}$$

Appendix B

Specifications of the Tecnotion TL-6N PMLSM

Table B.1: Specifications of Tecnotion TL-6N PMLSM [11]

	value
Motortype, max voltage ph-ph	3-phase synchronous Ironcore, 600 Veff
Ultimate Force @25°	450 N
Ultimate Current	6.5 A
Peak Force @25°	400 N
Peak Current	5.0 A
Continuous Force watercooled @100°	210 N
Continuous Current watercooled	2.3 A
Continuous Force aircooled @100°	100..200 N
Max. Continuous Power Loss	155 W
Maximum Speed @560V	5 m/s
Motor Force Constant	93 N/Arms
Back EMF	76 V / m/s
Motor Constant	370 N^2 / W
Magnet Pitch NN	24 mm
Resistance per phase	7.8 Ω
Induction per phase	60 mH
Electrical time constant	7.5 ms
Thermal Resistance	0.48 °C/W
Thermal time constant	77 s
Motor Attraction Force	900 N
Length of Coil unit	146 mm
Weight of Coil unit	1.5 kg
Weight of Cables	180 gr/m
Watercooling flow	0.7 l/min
Watercooling pressuredrop	1 bar
Temperature Sensor	PTC 1 kΩ

Appendix C

List of symbols

Table C.1: List of symbols

symbol	description	unit
ρ	free charge density	C/m^3
τ_S	slot pitch	m
τ_P	pole pitch	m
ψ_n	flux linkage in phase n	Wb
$\hat{\psi}$	amplitude of flux linkage	Wb
a	acceleration of the translator	m/s^2
$\vec{B}$	magnetic flux density	T
$C(s)$	controller transfer function	N/m
D	damping	N / m/s
$\vec{D}$	electric flux density	C/m^2
d_n	distance between stator segment S_n and S_{n-1}	m
$\vec{E}$	electric field strength	V/m
e_n	EMF induced in phase n	V
F_{cog}	cogging force	N
F_k	thrust force	N
F_r	reluctance force	N
g	airgap length	m
$\vec{H}$	magnetic field strength	A/m
i_n	current in phase n	A
$\vec{J}$	magnetic polarization	T
$\mathbf{k}$	force function matrix	N/A, A, A
k_n	force function for phase n	N/A
L_n	self-inductance in phase n	H
L_{sn}	synchronous inductance in phase n	H
L_S	stator length	m
L_T	translator length	m
M_{mn}	mutual-inductance between phases m and n	H
m	mass	kg
$P(s)$	motor transfer function	m/A
P_{mech}	mechanical power	W
P_n	power in phase n	W
R	ohmic resistance of the coil	Ω
S_n	stator segment n	-
$\mathbf{T}$	$dq0$-transformation matrix	-
t	time	s
V	voltage	V
v	velocity of the translator	m/s
W_m	magnetic energy	J
x	position of the translator	m

Bibliography

[1] J. F. Gieras and Z. Piech, *Linear Synchronous Motors.* CRC Press, 2000.

[2] D. Hanselman, *Brushless Permanent Magnet Motor Design.* The Writers' Collective, 2003.

[3] J. Jansen, E. Lomonova, A. Vandenput, J. Compter, and A. Verweij, "Improvement of the dynamic performance of an ac linear permanent magnet machine," *Electric Machines and Drives Conference, 2003. IEMDC'03. IEEE International*, vol. 2, pp. 785–790, 2003.

[4] D. Krop, E. Lomonova, and A. Vandenput, "Application of schwarz-christoffel mapping to permanent-magnet linear motor analysis," *IEEE Transactions on Magnetics*, vol. 44, pp. 352–359, 2008.

[5] E. P. Furlani, *Permanent Magnet and Electromechanical Devices.* Academic Press, 2001.

[6] H. W. Beaty and J. L. J. Kirtley, *Electric Motor Handbook.* McGraw-Hill Handbooks, 1998.

[7] B.-G. Gu and K. Nam, "A vector control scheme for a pm linear synchronous motor in extended region," *IEEE Transactions on Industry Applications*, vol. 39, pp. 1280–1286, 2003.

[8] C. M. M. van Lierop, J. W. Jansen, A. A. H. Damen, and P. P. J. van den Bosch, "Control of multi-degree-of-freedom planar actuators," *Proceedings of the IEEE International Conference on Control Applications*, pp. 2516–2521, 2006.

[9] C. R. Rao and S. K. Mitra, *Generalized Inverse of Matrices and its Applications.* Wiley, 1971.

[10] M. Steinbuch, "Control for dummies," 2001.

[11] Tecnotion, http://www.tecnotion.com/ProductsIncludeFiles/Downloads/leaflet_tl.pdf, *Tecnotion Tl-6N specifications.*